

Wingtip-Mounted Propellers: Aerodynamic Analysis of Interaction Effects and Comparison with Conventional Layout

Tomas Sinnige,* Nando van Arnhem,[†] Tom C. A. Stokkermans,[†] Georg Eitelberg,[‡] and Leo L. M. Veldhuis[‡]

Delft University of Technology, 2629 HS Delft, The Netherlands

DOI: 10.2514/1.C034978

Wingtip-mounted propellers installed in a tractor configuration can decrease the wing induced drag by attenuating the wingtip vortex by the propeller slipstream. This paper presents an aerodynamic analysis of the propeller–wing interaction effects for the wingtip-mounted propeller configuration, including a comparison with a conventional configuration with the propeller mounted on the inboard part of the wing. Measurements were taken in a low-speed wind tunnel at Delft University of Technology, with two wing models and a low-speed propeller. Particle-image-velocimetry measurements downstream of a symmetric wing with integrated flap highlighted the swirl reductions characteristic of the wingtip-mounted propeller due to wingtip-vortex attenuation and swirl recovery. External-balance and surface-pressure measurements confirmed that this led to an induced-drag reduction with inboard-up propeller rotation. In a direct comparison with a conventional propeller–wing layout, the wingtip-mounted configuration showed a drag reduction of around 15% at a lift coefficient of 0.5 and a thrust coefficient of 0.12. This aerodynamic benefit increased upon increasing the wing lift coefficient and propeller thrust setting. An analysis of the wing performance showed that the aerodynamic benefit of the wingtip-mounted propeller was due to an increase of the wing's effective span-efficiency parameter.

Nomenclature

\mathcal{R}	= wing aspect ratio, b^2/S
b	= wingspan, 2s, m
C_D	= drag coefficient, $D/q_\infty S$
$C_{D_{\min}}$	= minimum drag coefficient
C_L	= lift coefficient, $L/q_\infty S$
$C_{L_{C_{D_{\min}}}}$	= lift coefficient at minimum drag coefficient
C_{L_α}	= lift-curve slope, 1/deg
C_P	= propeller power coefficient, $P/\rho_\infty n^3 D^5$
C_p	= static-pressure coefficient, $(p - p_\infty)/q_\infty$
C_{p_t}	= total-pressure coefficient, $(p_t - p_\infty)/q_\infty$
C_T	= propeller thrust coefficient, $T/\rho_\infty n^2 D^4$
c	= wing chord length, m
c_{d_p}	= section pressure-drag coefficient, $d_p/q_\infty c$
c_l	= section lift coefficient, $l/q_\infty c$
D	= drag force, N; propeller diameter, m
d_p	= pressure-drag force per unit span, N/m
$d\Gamma$	= shed circulation due to spanwise lift gradient, m^2/s
e	= span-efficiency parameter
J	= propeller advance ratio, V_∞/nD
L	= lift force, N
l	= lift force per unit span, N/m
n	= propeller rotational speed, Hz
P	= propeller power, W
p	= static pressure, Pa
p_t	= total pressure, Pa

q	= dynamic pressure, $\rho V^2/2$, Pa
R	= propeller radius, m
Re_c	= Reynolds number based on pylon chord, $V_\infty c/\nu$
Re_D	= Reynolds number based on propeller diameter, $V_\infty D/\nu$
r	= radial coordinate, m
S	= wing reference area, m^2
s	= wing semispan, m
T	= propeller thrust, N
V	= velocity, m/s
V_a	= axial velocity, m/s
V_t	= tangential velocity, m/s
X, Y, Z	= streamwise, spanwise, and vertical coordinates in wing-based coordinate system, m
X_p, Y_p, Z_p	= streamwise, spanwise, and vertical coordinates in propeller-based coordinate system, m
α	= angle of attack, deg
ΔC_{D_i}	= difference in drag coefficient due to wingtip-mounted configuration, $C_{D_i} - C_{D_c}$
ΔC_{p_i}	= rise in total-pressure coefficient due to propeller, $C_{p_i}^{P-on} - C_{p_i}^{P-off}$
$\overline{\Delta C_{p_i}}$	= circumferentially averaged rise in total-pressure coefficient due to propeller
δ_f	= flap deflection angle, deg
η_p	= propeller efficiency, $J C_T / C_P$
θ	= swirl angle, $\tan^{-1}(V_t/V_a)$, deg
ν	= kinematic viscosity, m^2/s
ρ	= air density, kg/m^3
ϕ	= circumferential blade position, deg

Received 21 February 2018; revision received 25 June 2018; accepted for publication 29 July 2018; published online 16 November 2018. Copyright © 2018 by T. Sinnige, N. van Arnhem, T. C. A. Stokkermans, G. Eitelberg, and L. L. M. Veldhuis. Published by the American Institute of Aeronautics and Astronautics, Inc., with permission. All requests for copying and permission to reprint should be submitted to CCC at www.copyright.com; employ the ISSN 0021-8669 (print) or 1533-3868 (online) to initiate your request. See also AIAA Rights and Permissions www.aiaa.org/randp.

*Ph.D. Candidate, Flight Performance and Propulsion Section, Faculty of Aerospace Engineering, Kluyverweg 1; T.Sinnige@tudelft.nl. Member AIAA.

[†]Ph.D. Candidate, Flight Performance and Propulsion Section, Faculty of Aerospace Engineering, Kluyverweg 1. Member AIAA.

[‡]Full Professor, Flight Performance and Propulsion Section, Faculty of Aerospace Engineering, Kluyverweg 1. Member AIAA.

Subscripts

c	= conventional configuration
IU	= inboard-up propeller-rotation case
OU	= outboard-up propeller-rotation case
s	= symmetric configuration
t	= wingtip-mounted configuration
∞	= freestream

Superscripts

P-off	= propeller-off
P-on	= propeller-on

I. Introduction

PROPELLER propulsion systems can enable a step-change improvement in fuel consumption and emissions of future passenger aircraft. The high effective bypass ratio associated with the propeller provides an inherent efficiency benefit compared to a turbofan engine of equivalent technology level. However, the integration of the propellers with the airframe remains a challenge, driving today's research on propellers. The recent focus on hybrid-electric propulsion [1] strengthens the need for propeller integration studies. The use of electric motors increases the design flexibility by practically eliminating potential penalties of downscaling the motors [2]. This enables novel configurations involving, for example, distributed propellers, for which successful airframe-propulsion integration is especially relevant. The NASA X-57 [3,4] is a prime example of such a configuration.

Conventionally, propellers are mounted to the wing in a tractor layout, with the propeller positioned on the inboard part of the wing. The aerodynamic interactions occurring for such a configuration have been the topic of extensive research studies [5–8], and can be divided into upstream and downstream effects. The upstream effect, referring to the influence of the wing on the propeller performance, is due to upwash and blockage caused by the lifting wing. As a result, the propeller experiences a nonuniform inflow, which leads to cyclic load fluctuations and potentially an associated noise penalty. The downstream effect is due to the interaction of the propeller slipstream with the wing. The increased dynamic pressure and swirl in the slipstream modify the lift and drag distributions over the entire wing, with the strongest effects occurring on the part of the wing immersed in the propeller slipstream. The lift is increased behind the upgoing blade due to the combined effects of the local propeller-induced upwash and dynamic-pressure rise, whereas behind the downgoing blade the lift typically decreases compared to the propeller-off result due to the propeller-induced downwash. The lift vector is tilted forward on the part of the wing that experiences a propeller-induced upwash; this leads to decreased induced drag, a phenomenon that can be explained as swirl recovery [8]. In case of positive wing lift, this is partially offset by the increase in induced drag on the part of the wing downstream of the downgoing blade side. Furthermore, the higher local dynamic pressure increases the viscous drag over the entire extent of the wing washed by the propeller slipstream.

The increased design flexibility offered by technologies such as hybrid-electric propulsion enables novel approaches to positioning the propellers on the aircraft, which can lead to significant integration benefits. The wingtip-mounted propeller is an example of such an approach. Already in the 1960s, Snyder and Zumwalt [9] showed that wingtip-mounted tractor propellers can decrease the wing drag, while increasing the wing's maximum lift coefficient and effective aspect ratio. These aerodynamic benefits are obtained when the propeller rotation direction is opposite to that of the wingtip vortex, thereby attenuating the wingtip vortex, and thus, reducing the downstream swirl. This was confirmed later by both experimental [8] and numerical [10] studies. A similar beneficial interaction occurs for the

pusher variant, for which the preswirled inflow to the propeller leads to a reduction of the required shaft power, while the wing induced drag may also be decreased due to the modification of the downstream vortex field [11,12].

So far, aeroelastic problems, high wing mass imposed by inertia loads, and insufficient control power to overcome a one-engine inoperative condition have prevented the use of wingtip-mounted propellers. However, with the advent of more electric aircraft configurations, the wingtip-mounted propeller becomes a feasible design option for future aircraft. By downscaling the motors and propellers, the major drawbacks of the wingtip-mounted propeller configuration may be overcome. At present, the literature lacks comprehensive analyses of the aerodynamic interaction effects relevant to the wingtip-mounted propeller, which are of crucial importance to fully exploit the configuration's potential aerodynamic benefits. The goal of this paper is to address this knowledge gap by providing a detailed aerodynamic analysis of the wingtip-mounted configuration, including integral and local force measurements, and comprehensive flowfield evaluations. Subsequently, the aerodynamic performance of the wingtip-mounted propeller configuration is compared to a conventional configuration, with the propeller mounted on the inboard part of the wing. The resulting data set provides insight into the interaction phenomena for conventionally mounted and wingtip-mounted propellers, and the mechanisms leading to the performance benefits of wingtip-mounted propellers.

An experimental approach was chosen to allow for rapid parameter sweeps to assess the sensitivity of the interaction effects to the angle of attack, propeller thrust setting, and propeller rotation direction. Furthermore, no data have been available so far for the validation of a numerical study of wingtip-mounted propellers. The data discussed in this paper can be used for code benchmarking, thereby aiding in the validation of numerical tools useful for both analysis and design purposes. Note that tip-mounted propellers also arise in other aircraft configurations, featuring pylon-mounted or horizontal-tailplane-mounted propellers. Although the interaction effects for such configurations are similar to those for the wingtip-mounted case, the aerodynamic performance goals are typically different and less focused on tip-vortex attenuation. Therefore, this paper focuses on the wingtip-mounted case only.

II. Experimental Setup

A. Wind-Tunnel Facility

The experiments were performed in the Low-Turbulence Tunnel at Delft University of Technology. This low-speed closed-return wind tunnel features a closed-wall test section, shown in Fig. 1, with a cross section of 1.80×1.25 m. At the selected freestream velocity of 40 m/s, the turbulence level is below 0.1%. The models were attached to a ground board of 2.055 m length suspended from the test section's ceiling, spanning the entire width of the test section. This ground board represents the symmetry plane for the experimental arrangement and reduced the height of the test section to 0.995 m.

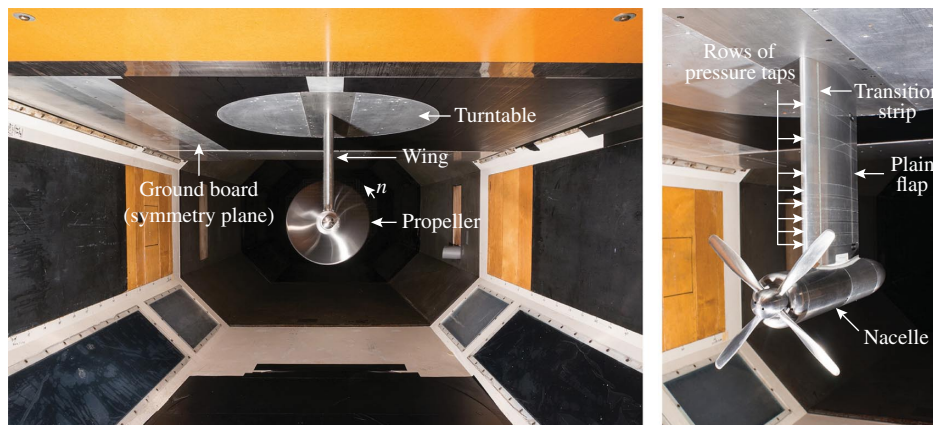


Fig. 1 Model 1 (symmetric wing with flap) installed in the wind tunnel.

The flow on the ground board was made turbulent by a transition strip, applied at 0.140 m from the board's leading edge. A turntable was integrated into the ground board to allow for measurements at nonzero angle of attack.

B. Models

1. Propeller Model

The propeller (Fig. 1) had a diameter of 0.237 m, and its four blades were set to a blade pitch angle of 23.9 deg at 75% of the radius (with the pitch angle defined relative to the local chord line). The radial distributions of the blade chord and pitch angle are provided in Ref. [13]. Compared to modern designs, the propeller had a low blade count, a low solidity, and no sweep. Still, its slipstream introduced all the relevant aerodynamic phenomena to the flowfield that affect the propeller–wing interaction. Therefore, the model was considered adequate for the current investigation. The propeller was driven by a 5.5 kW three-phase induction motor housed inside an axisymmetric nacelle with a diameter of 0.070 m, which was connected directly to the wing models described later.

Because the propeller was not instrumented, reference measurements of the isolated propeller performance were taken with a sting-mounted configuration. A CAD model of this setup is attached to the paper as Supplemental Data S1. The sting was connected directly to an external balance (discussed in Sec. II.C.1), with the height of the sting selected such that the propeller was positioned in the middle of the wind tunnel. A test section without ground board had to be used, which was considered acceptable because, in this case, the balance measurements did not include the forces acting on the turntable. A separately supported streamlined sleeve, not connected to the external balance, was installed around the sting to eliminate measurement error due to the interaction of the sting with the propeller slipstream. The forces on the nacelle were included in the thrust measurements. Tare runs were taken with a dummy spinner (blades off) and subtracted from the propeller-on data to isolate the blade forces, neglecting the nacelle interference-drag component caused by the interaction with the propeller slipstream. The axial spacing between the sleeve's leading edge and the propeller plane (1.5 times the propeller diameter) was sufficient to prevent an upstream effect on the propeller performance.

2. Wing Models

Semi-installed propeller–wing configurations were simulated by connecting the tractor propeller with nacelle to two different wing models. A straight wing with a symmetric airfoil, an integrated flap, and pressure taps (model 1) was used for a detailed investigation of the wingtip-vortex-attenuation and swirl-recovery mechanisms occurring for the wingtip-mounted configuration. A straight, modular wing with a cambered airfoil (model 2) was tested to compare the aerodynamic performance of the wingtip-mounted configuration and the conventional configuration (with the propeller mounted on the inboard part of the wing). The wing models were connected to the turntable integrated into the ground board, with the wing leading edge positioned at 1.205 m (5.02c) downstream of the ground board's leading edge.

a. Model 1: Symmetric Wing with Integrated Flap. Figure 1 provides photographs of the model configuration with the symmetric wing (referred to as model 1) installed in the test section, whereas Figs. 2 and 3 display the corresponding technical drawings. CAD models of the setup are attached to this paper as Supplemental Data S2. The nacelle was connected to a straight, untapered wing with a chord length of 0.240 m, a span of 0.292 m, a symmetric NACA 64₂A015 profile, and an integrated 25%-chord plain flap with a flap gap of 1 mm. This low-aspect-ratio wing with a high ratio of propeller diameter to wingspan was chosen to obtain a relatively strong interaction between the propeller slipstream and the wing, which aided in the interpretation of the aerodynamic interaction mechanisms. Transition was forced using strips with silicon-carbide particles, positioned at $X/c = 0.12$ on both the upper and lower sides of the wing. Chordwise rows of static-pressure taps were available at eight spanwise locations, as discussed in Sec. II.C.2. The spacing between the propeller plane and the wing leading edge was fixed at 44% of the propeller diameter.

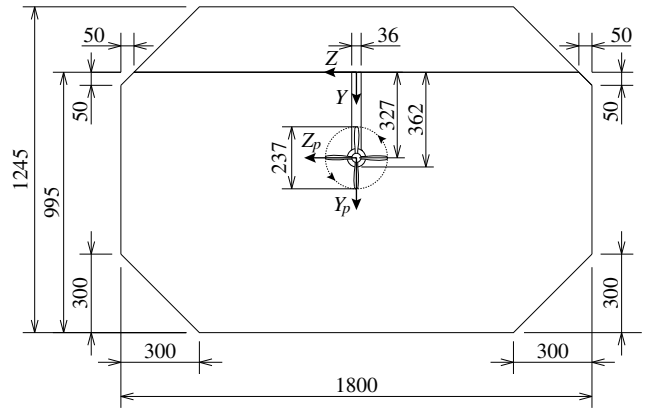
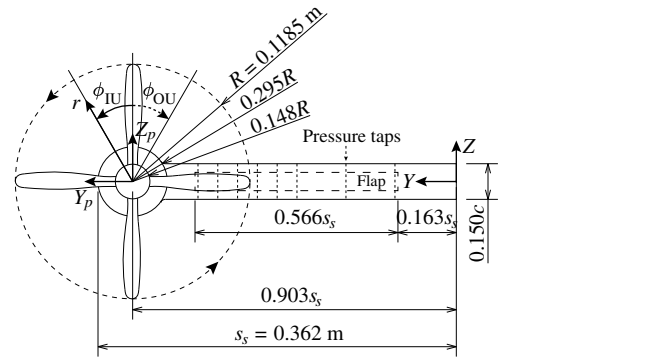
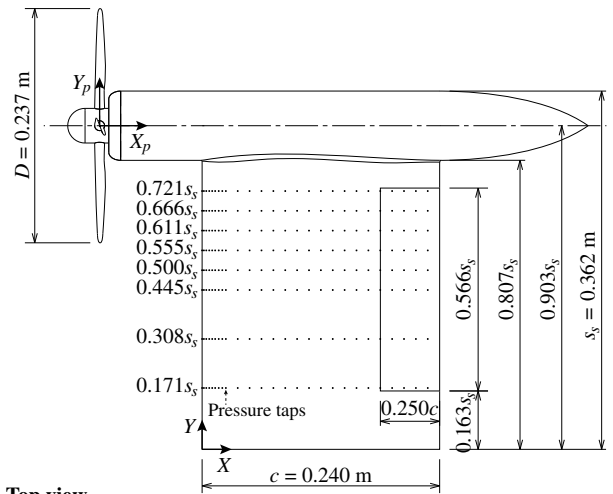


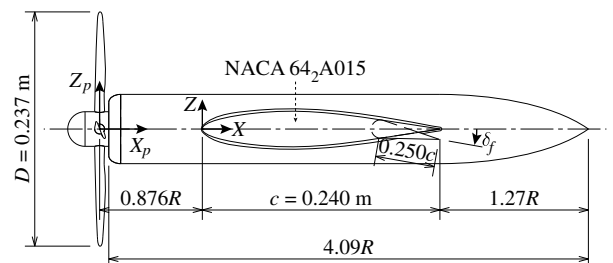
Fig. 2 Overview technical drawing of model 1 installed in the wind tunnel.



a) Front view



b) Top view



c) Section view

Fig. 3 Detailed technical drawings of model 1.

The flap was used to simulate the cases with the propeller slipstream rotating in the same and opposite directions of the wingtip vortex (outboard-up and inboard-up propeller rotation) with a single propeller model. This was achieved by running the tests at positive

and negative flap deflection angles ($\pm 10^\circ$). The results obtained at the negative flap deflection were inverted during postprocessing by changing the sign of the angle of attack and the lift coefficient to represent the outboard-up rotating case at the positive flap setting:

$$\begin{aligned}\alpha_{OU} &= -\alpha_{IU} \\ C_{L_{OU}} &= -C_{L_{IU}} \\ C_{D_{OU}}(C_{L_{OU}}) &= C_{D_{IU}}(-C_{L_{IU}})\end{aligned}\quad (1)$$

Because the flap only covered the spanwise extent from $Y/s_s = 0.163$ to $Y/s_s = 0.729$, the lift distribution will have differed somewhat from that on a wing with equal planform, but having a cambered airfoil profile. The vorticity shed from the flap side edges causes a reduction in circulation of the wingtip vortex for the case with flap. This may have slightly reduced the magnitude of the interaction effects compared to a more representative cambered wing without flap. However, comparisons with a short-span version of the modular cambered wing model discussed next showed that the general trends for the inboard-up rotation case were the same as measured with the model with flap, at all considered propeller operating conditions. Therefore, it was concluded that the model with flap was adequate to study the aerodynamic phenomena relevant to the wingtip-mounted propeller configuration.

b. Model 2: Modular Cambered Wing. Figure 4 displays photographs of the modular cambered wing (referred to as model 2) in the conventional and wingtip-mounted configurations, of which technical drawings are provided in Figs. 5 and 6. CAD models of the setup are attached to this paper as Supplemental Data S3. The straight and untapered wing consisted of two spanwise segments, which could be installed such that the nacelle was positioned in between both segments (conventional configuration) or at the tip of the two segments combined (wingtip-mounted configuration). The wing chord length

was the same as for model 1 (0.240 m), while a modified NACA 64₂A615 profile was chosen to achieve a lift coefficient of around $C_L = 0.3$ at $\alpha = 0^\circ$. For manufacturing reasons, the trailing-edge thickness was increased to $8.3 \cdot 10^{-4}$ times the chord length. This resulted in a slight bulge in the aft part of the profile (around $X/c = 0.9$), which may have promoted separation. Transition was fixed using strips with the same silicon-carbide particles as used for model 1, in this case installed at $X/c = 0.08$ on both the upper and lower sides of the wing. The spacing between the propeller plane and the wing leading edge was fixed at 43% of the propeller diameter (approximately the same as for model 1), while the wing was oriented such that the propeller–wing combination featured inboard-up rotation.

The conventional configuration had a rounded tip and a semispan of 0.748 m ($R = 6.2$), leading to a ratio of propeller diameter to wing semispan of 0.32, a typical value according to the twin-engine propeller-aircraft database provided in Ref. [8]. The span of the inboard wing segment was approximately equal to the total span of model 1. As a result, the propeller axis was positioned at $Y/s_c = 0.444$, which is somewhat more outboard than the typical value of $Y/s = 0.30$ [8]. This was considered acceptable for the present study, because the spanwise loading gradient on the inboard part of the wing is relatively small. Therefore, the sensitivity of the propeller–wing interaction effects to the spanwise location of the propeller will be small as well on this part of the wing. The semispan of the wingtip-mounted configuration was 0.730 m up to the outboard edge of the nacelle ($R = 6.1$), with a spanwise propeller position of $Y/s_t = 0.952$. Although the location of the propeller with respect to the wind-tunnel walls differed between the conventional and wingtip-mounted configurations, it was assumed that the propeller performance was the same for both cases. This was confirmed by previous work focusing on propeller aerodynamics in close ground proximity [14], which showed that propeller performance remains unaffected by wall spacing for spacing values above 1.5 times the propeller radius.

C. Measurement Techniques

Table 1 provides an overview of the measurement techniques applied for the tests with models 1 and 2. The experimental data were not corrected for wind-tunnel wall effects and buoyancy effects.

1. External Balance

The integral forces and moments generated by the propeller–wing combinations were obtained with an external six-component balance. Measurements were taken both with and without the propeller blades installed to allow for an assessment of the aerodynamic interaction effects caused by the propeller slipstream. A simple bookkeeping procedure was followed to separate the forces and moments generated by the wing with nacelle and the propeller. To this end, the isolated propeller's performance data were used, as measured with the sting-mounted configuration. In this process, the upstream effect of the wing on the propeller performance was neglected. Apart from the forces acting on the models, the balance data also included the forces and moments on the turntable in the wind-tunnel ceiling, mostly dominated by skin-friction drag. Tare measurements were taken with the models removed from the test section to correct for this effect. This approach

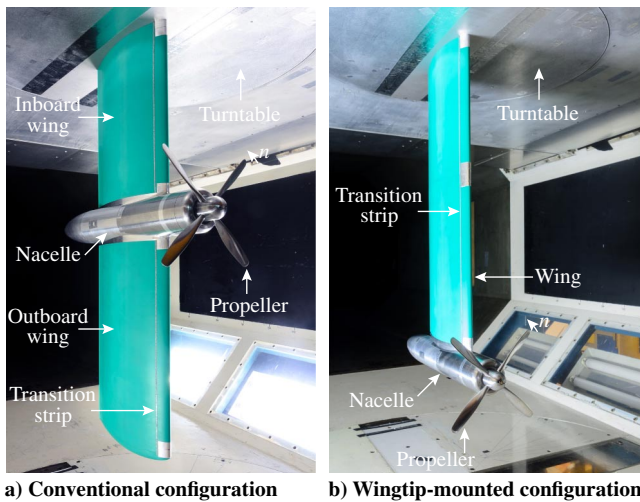


Fig. 4 Model 2 installed in the wind tunnel.

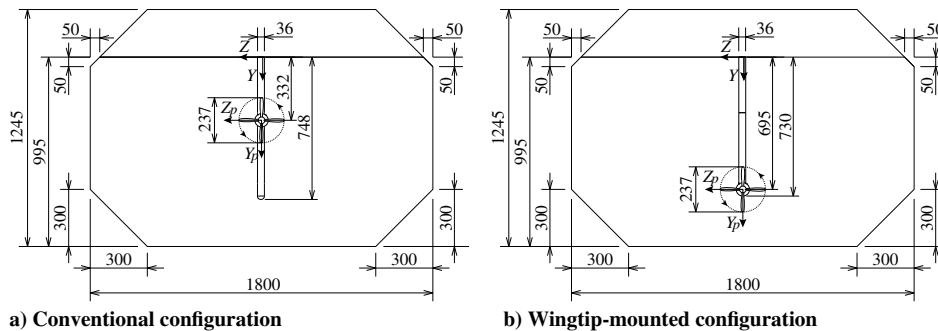


Fig. 5 Overview technical drawings of model 2 installed in the wind tunnel.

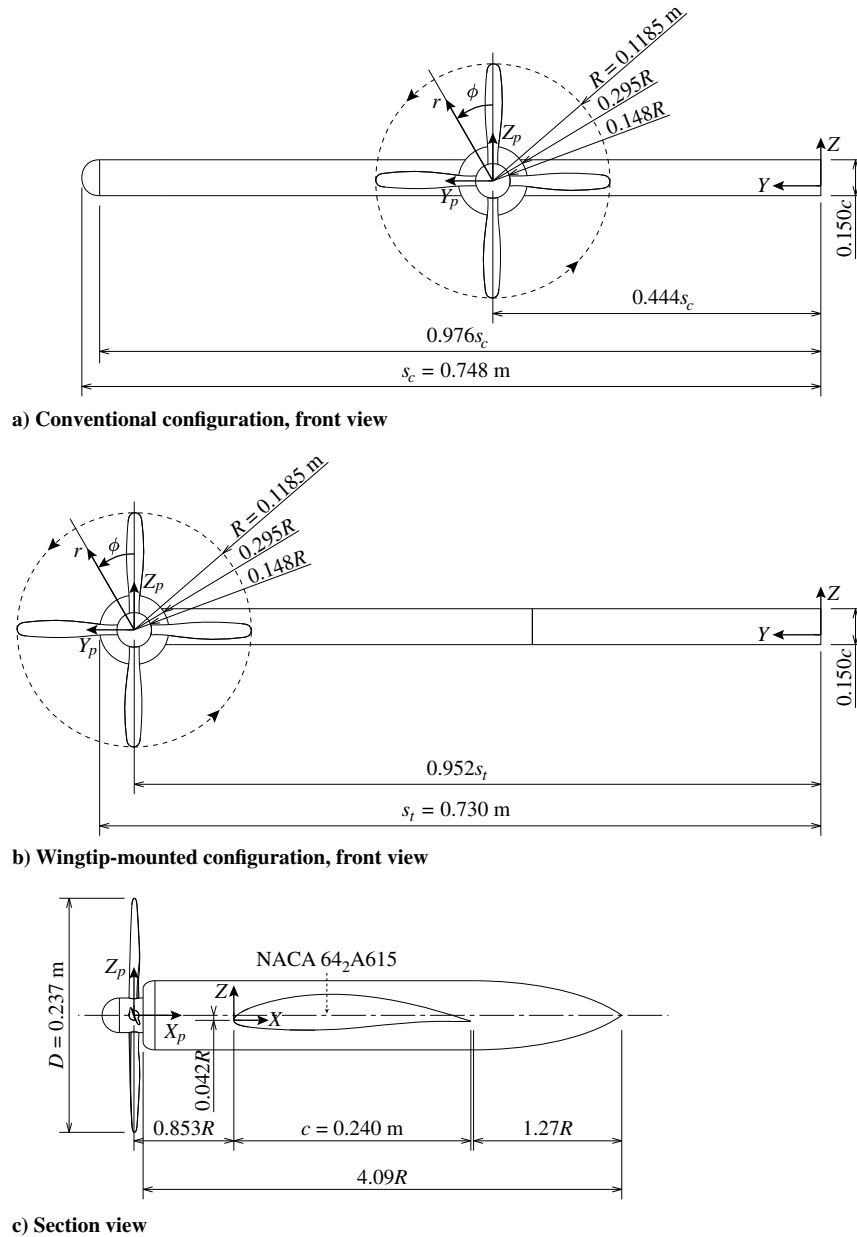


Fig. 6 Detailed technical drawings of model 2.

cannot account for the interference drag associated with the junction flow at the interface between the wing and the turntable. The uncertainty of the balance measurements was estimated from repeated measurements at equal operating conditions. The standard deviation of the lift data was 0.04 lift counts, whereas the standard deviation of the drag data was 3 drag counts.

2. Pressure Taps

The symmetric wing model contained a total of 408 pressure taps (Fig. 3b), providing local measurements of the pressure distribution at

eight spanwise locations: $Y/s_s = [0.171, 0.308, 0.445, 0.500, 0.555, 0.611, 0.666, 0.721]$. The pressure taps were cross-connected in the spanwise direction at each chordwise position. Therefore, the measurements were taken per chordwise pressure row, with all other rows closed by tape. The pressures from each chordwise row were simultaneously recorded at a sampling rate of 5 Hz using an electronic pressure scanner, and averaged over time to obtain the final results per data point. The pressure data were integrated to obtain the section lift and pressure-drag coefficients on the wing. In this process, the local geometry of the wing profile was accounted for.

3. Particle-Image Velocimetry

Flowfield measurements were taken using stereoscopic particle-image velocimetry (PIV) in the wake of model 1. Table 2 provides an overview of the measurement and postprocessing characteristics of the PIV setup, whereas Fig. 7 illustrates the position of the PIV plane with respect to the model. The laser and cameras were traversed simultaneously in the vertical direction to allow for measurements in three different planes, oriented perpendicularly to the freestream flow direction at $1.5c$ downstream of the wing trailing edge ($X/c = 2.5$). The results from the three measurement planes were combined in

Table 1 Measurement techniques applied for the tests with models 1 and 2

Measurement technique	Measurement aim	Model 1	Model 2
External balance	Integral loading	Yes	Yes
Pressure taps	Sectional wing loading	Yes	No
PIV	Wingtip-vortex attenuation	Yes	No
Wake rake	Slipstream deformation	Yes	Yes
Total-pressure probe	Propeller total-pressure rise	Yes	No
Oil-flow visualization	Flow separation	No	Yes

Table 2 Measurement and postprocessing characteristics of the stereoscopic PIV setup

Parameter	Value
PIV setup	Stereoscopic
Laser	200 mJ Nd: YAG
Cameras	2 × 16 Mpixel CCD sensor
Objective	200 mm $f/4$
FOV size, mm	360 × 485
FOV position (X/c)	2.5
Pulse separation, μ s	40
Maximum particle displacement, pixel	25
Image pairs	1000
Final interrogation window size, pixel	24 × 24
Window overlap factor, %	50
Vector spacing, mm	0.9
Uncertainty instantaneous velocity magnitude	0.018 V_∞
Uncertainty mean velocity magnitude	0.001 V_∞

CCD = charge-coupled-device.

postprocessing to obtain a final field of view (FOV) with dimensions of 360 × 485 mm, which covered the entire wake of the propeller–wing model. Both phase-uncorrelated and phase-locked measurements were taken; the present paper only considers the phase-uncorrelated data. Postprocessing was performed with an iterative multigrid approach [15], and the uncertainty of the instantaneous velocity components was computed with the method by Wieneke [16]. The statistical uncertainty of the mean velocity components was obtained from the variations between uncorrelated samples at each vector location and the local number of samples available for averaging. Table 2 lists the uncertainty values averaged over the FOV; the uncertainty of the velocity components near the slipstream edge was up to three times larger due to the local effect of the propeller-blade tip vortices. Besides the contribution due to uncertainty of the instantaneous velocity fields, the statistical uncertainty of the mean also contains a contribution due to turbulence.

4. Wake Rake

A traversable wake rake was used to map the total-pressure distribution in the wake of the models at the same axial position as the PIV plane ($X/c = 2.5$). For model 2, only total-pressure measurements were taken, with a resolution of 3 mm in the lateral and vertical directions. For model 1, the spatial resolution was increased to 2 mm, while static-pressure measurements were taken with a resolution of 4 mm. The traversing range was selected such that the wing and nacelle wakes and the propeller slipstream were positioned entirely inside the FOV. The pressures at all probe locations were recorded simultaneously with the same electronic pressure scanner as used for the surface-

pressure measurements with pressure taps. Because the maximum swirl angle in the wake of the models was approximately 12 deg, a maximum error of about 2% occurred due to local misalignment of the probe [17]. The wake rake was removed from the test section during all other measurements to prevent an unwanted upstream effect on the wing and propeller performance.

5. Total-Pressure Probe

A circular, square-ended total-pressure probe with a diameter of 1.5 mm was used to measure the total-pressure rise induced by the propeller. Measurements were taken both for the sting-mounted propeller and model 1 (symmetric wing) to study the upstream effect of the wing on the propeller loading. The probe was designed such that it could provide measurements of the propeller loading distribution in the region upstream of the wing, with the tip of the probe positioned at 0.15 R downstream of the propeller center. The maximum swirl angle in the propeller slipstream at the measurement location was about 8 deg, leading to a maximum error of less than 0.5% due to local misalignment of the probe [17]. The probe and its support infrastructure were removed from the test section during all other measurements. Data were acquired over the entire propeller disk by traversing the probe in the radial and circumferential directions, with a radial resolution of 3 mm (0.025 R) and a circumferential resolution of 10 deg. This full measurement grid was only considered for the wing-installed configuration at $J = 0.8$. At the other advance ratios, the full radial range was measured only at $\phi = [0, 90, 180, 270]$ deg, whereas the full circumferential range was only covered at $r/R = 0.76$. Considering the expected axisymmetry of the sting-mounted propeller, for this configuration, only circumferential angles in the range of $90 \leq \phi \leq 270$ deg were evaluated.

6. Oil-Flow Visualization

Surface-flow visualizations were performed using a fluorescent oil technique [18] on the upper surface of model 2 (modular cambered wing). Following each data point, the tunnel was stopped and the oil was redistributed over the model. The visualizations were performed to identify the flow-separation pattern over the wing and nacelle, with and without the propeller running. Furthermore, the effectiveness of the transition strips could be verified.

D. Test Cases

The majority of the measurements discussed in this paper were taken at a freestream velocity of $V_\infty = 40$ m/s. This velocity provided the best compromise between the achievable Reynolds number and the operating range of the propeller, which was constrained by the output power of the electric motor. The resulting Reynolds number based on the wing chord was about $Re_c = 650,000$, whereas the Reynolds number based on the propeller diameter was $Re_D = 640,000$. The propeller was operated at four thrust settings, corresponding to advance ratios J of 0.7, 0.8, 0.9, and 1.0. The associated thrust coefficients C_T were equal to 0.123, 0.095, 0.053, and 0.014, respectively, while the Reynolds number at $r/R = 0.7$ was in the range of 130,000–180,000 (for $J = 1.0$ down to $J = 0.7$). For model 2, additional measurements were taken at $V_\infty = 28$ m/s to achieve higher thrust coefficients. At this velocity, the propeller was also operated at advance ratios of 0.5 and 0.6, resulting in thrust coefficients of 0.168 and 0.144, respectively. The corresponding Reynolds numbers were 455,000 based on the wing chord; 450,000 based on the propeller diameter; and 90,000–170,000 based on the effective velocity and chord at $r/R = 0.7$ (for $J = 1.0$ down to $J = 0.5$). The sting-mounted propeller data were acquired at Reynolds numbers of $Re_D = 620,000$ and $Re_D = 470,000$. The difference in Reynolds number of at most 4% between the sting-mounted and wing-installed measurements is ignored in the evaluations discussed in this paper. For all configurations, tare measurements were taken with the blades removed to obtain a baseline to which the propeller-on data could be compared.

Compared to high-speed propellers with high disk loading, the considered thrust coefficients are relatively low, thus making the test cases particularly representative of smaller vehicles with low-speed

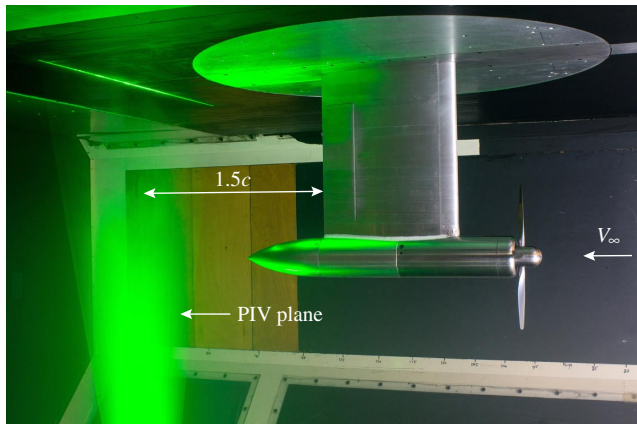


Fig. 7 Position of the PIV plane with respect to the model.

propellers. Considering that the wingtip-mounted propeller is especially feasible for aircraft with (distributed) electric propulsion, this was considered acceptable.

The aerodynamic performance measurements with the external balance and surface-pressure taps were taken over a range of angles of attack α at zero sideslip angle. For model 1, the angle of attack was varied over the range $-20 \leq \alpha \leq 20$ deg. For model 2, the angle-of-attack range was $-8 \leq \alpha \leq +15$ deg for the wingtip-mounted configuration and $-8 \leq \alpha \leq +10$ deg for the conventional configuration. For the latter case, the maximum angle of attack was limited because of the weaker connection between the nacelle and the outboard wing segment. The wake-rake, PIV, and propeller-slipstream evaluations with model 1 were intended to be performed at $\alpha = 0$ deg, but due to a small misalignment of the setup, the actual angle of attack was $\alpha = -0.2$ deg for the inboard-up case and $\alpha = +0.2$ deg for the outboard-up case. For model 2, the wake-rake data were acquired at $\alpha = 0$ deg and at a constant lift coefficient of $C_L = 0.5$. The misalignment of model 1 was resolved before performing the pressure and balance measurements discussed in this paper. The sting-mounted propeller was evaluated before the misalignment was resolved, and thus, the propeller performance data also suffered from a -0.2 deg misalignment. Interpolation was performed to obtain the propeller performance at the same angles of attack as the balance data acquired with models 1 and 2.

III. Results

A. Isolated Propeller Performance

The performance of the isolated propeller was determined as baseline for the wing-installed measurements discussed in the subsequent sections. The data were acquired with the sting-mounted configuration described in Sec. II.B.1, and are attached to this paper as Supplemental Data S4. Figure 8 provides the performance data and the radial distribution of the total-pressure rise downstream of the propeller as measured at $\alpha = -0.2$ deg and $Re_D = 620,000$. The performance data (Fig. 8a) feature markers at each individual data point recorded during the tests, together with curve fits through the thrust and power data. Third-order polynomials were used, because these resulted in the best fit through the data without introducing artifacts typical of higher-order fits. The fit through the propeller efficiency data was obtained by combining the polynomials computed for the thrust and power coefficients. The total-pressure data (Fig. 8b) were acquired at $\phi = 180$ deg.

Figure 8a displays the expected quasi-linear behavior of the thrust and power coefficients at low propeller loading conditions. The maximum propeller efficiency is limited to about 0.75, occurring at $J = 0.77$. The total-pressure data depicted in Fig. 8b demonstrate that this relatively low efficiency can be attributed to a total-pressure loss on the inboard part of the blades. Previous numerical simulations [19] showed that this total-pressure loss was due to flow separation on the locally inefficient blade cross sections.

To extend the range of attainable thrust coefficients, measurements with the sting-mounted propeller were also taken at a lower Reynolds

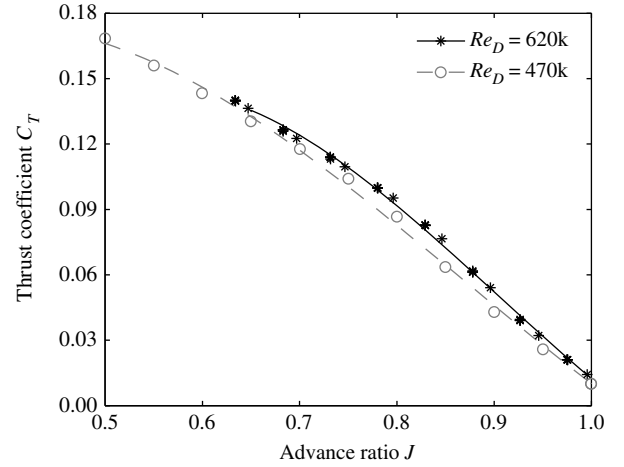


Fig. 9 Effect of Reynolds number on the propeller thrust at $\alpha = -0.2$ deg.

number of $Re_D = 470,000$. A third-order curve was again fit through the measurement data, as plotted in Fig. 9 together with the result obtained at $Re_D = 620,000$. The lowest advance ratio attainable at $Re_D = 470,000$ was equal to $J = 0.5$, at which a maximum thrust coefficient of $C_T = 0.168$ was achieved. At a given advance ratio, the reduction in Reynolds number of 25% led to a mean decrease in thrust coefficient of about 0.006 for the case at $Re_D = 470,000$ compared to the result at $Re_D = 620,000$.

When operating the propeller under asymmetric inflow conditions, the blade loading changes due to nonuniform inflow. For a positive angle of attack, the downgoing blade experiences an increase in loading, whereas the upgoing blade experiences a decrease in loading [8]. Figure 10 displays the effect of angle of attack on the time-averaged thrust coefficient, defined positive in the negative drag direction. At $J = 1.0$, the lowest thrust setting considered, the thrust coefficient increased by 0.027 when going from $\alpha = -0.2$ deg to $\alpha = 19.8$ deg. The sensitivity of the propeller thrust coefficient to the angle of attack decreases with increasing thrust setting because of the associated increase in rotational velocity of the blades. This decreases the angle-of-attack perturbation experienced by the blade sections at a given propeller angle of attack. At $J = 0.7$, the thrust was insensitive to the angle of attack over the entire range of inflow angles considered. The data shown in Fig. 10 are used in Sec. III.C.3 to isolate the forces on the wing from the overall system forces (which include the propeller loading).

B. Aerodynamic Interaction Effects for Wingtip-Mounted Propellers (Model 1)

The wingtip-vortex-attenuation and swirl-recovery mechanisms characteristic of the wingtip-mounted propeller were studied using model 1 (symmetric wing model with flap; see Figs. 1–3) at $Re_D = 640,000$. The measurement data are attached to this paper as

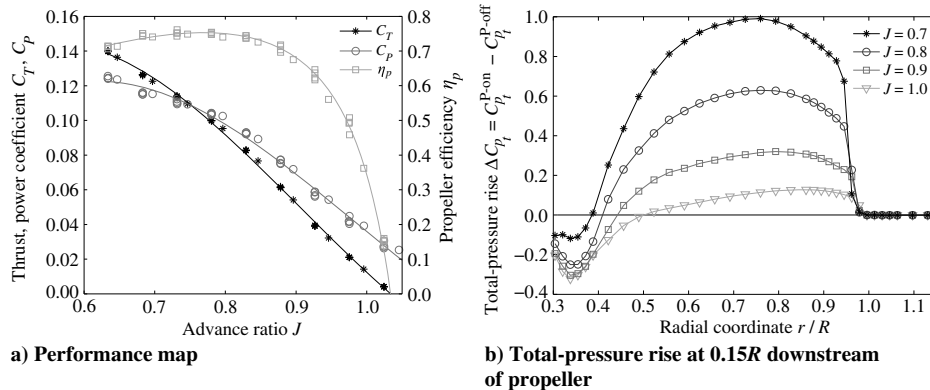


Fig. 8 Isolated propeller performance at $\alpha = -0.2$ deg and $Re_D = 620,000$.

Supplemental Data S5. As discussed in Sec. II.B.2.a, the inboard-up and outboard-up rotation cases were simulated with the same propeller model by deflecting the flap in the positive and negative directions, and inverting the data for the case with the negative flap deflection [Eq. (1)]. The data labeled as inboard-up and outboard-up with the propeller off represent the measurements taken with the positive and negative flap deflections without propeller installed. Considering the symmetry of the setup without propeller, the corresponding results should be the same.

1. Wingtip-Vortex Attenuation and Swirl Recovery

In the wingtip-mounted configuration, the propeller slipstream interacts with the flow around the wingtip. This strongly affects the induced drag of the wing, as will be shown in Sec. III.B.3. To assess the modification of the swirl due to the interaction between the propeller slipstream and the wingtip vortex, Fig. 11 provides contours of the swirl angle measured with PIV for the inboard-up and outboard-up rotation cases. The measurements were taken at $\alpha = -0.2$ deg for the inboard-up case and $\alpha = +0.2$ deg for the outboard-up case (due to a small misalignment), meaning that the lift coefficients differed between the considered operating conditions. The absolute value of the

Table 3 Effect of propeller rotation direction and thrust setting on the mean swirl angle in the wake of the propeller-wing model at $\alpha = -0.2$ deg (inboard-up) and $\alpha = +0.2$ deg (outboard-up)

Operating point		C_L		$1/(\pi(1.1R)^2) \int_0^{2\pi} \int_0^{1.1R} \theta r dr d\phi$	
J	C_T	Inboard-up	Outboard-up	Inboard-up, deg	Outboard-up, deg
Prop-off	—	0.16	0.18	-2.9	-3.0
1.0	0.014	0.16	0.18	-2.0	-3.5
0.9	0.053	0.18	0.17	-1.0	-4.5
0.8	0.095	0.21	0.16	-0.1	-5.4
0.7	0.123	0.25	0.14	+0.7	-6.3

swirl angle is shown in Fig. 11 to highlight the differences in magnitude of the swirl for both rotation directions. To compare the inboard-up and outboard-up rotation cases quantitatively, the mean swirl angle was computed over a circular domain enclosing the propeller slipstream. The outer integration limit was set to $1.1R$ to account for the slipstream distortion at the higher thrust settings. The corresponding results are listed in Table 3; note again that the lift coefficient varied between the different operating conditions considered.

Figure 11 shows that, despite the higher lift coefficients, the remaining swirl in the wake of the models is considerably lower with inboard-up rotation than with outboard-up rotation, at all thrust settings. For the inboard-up rotation case, the swirl in the propeller slipstream partially cancels the swirl associated with the wingtip vortex, whereas with outboard-up rotation, these two contributions are in the same direction, and hence, the total swirl is amplified. This is substantiated by Table 3, which highlights that, with inboard-up rotation, the negative swirl of the wingtip vortex is increasingly compensated for by the positive swirl contribution by the propeller when increasing the thrust setting. With outboard-up rotation, on the other hand, the swirl angle becomes increasingly negative with increasing thrust setting. Apart from the modification of the mean swirl, Fig. 11 also shows that the interaction between the propeller slipstream and the wingtip vortex changes the swirl in the vicinity of the wingtip-vortex core (near $Y_p/R = Z_p/R = 0$). With inboard-up rotation, the local maximum in swirl is decreased, confirming the existence of the wingtip-vortex-attenuation mechanism. For the case with outboard-up rotation, a strong maximum in swirl occurred near the flap edge due to the combined effects of the flap-edge vortex and

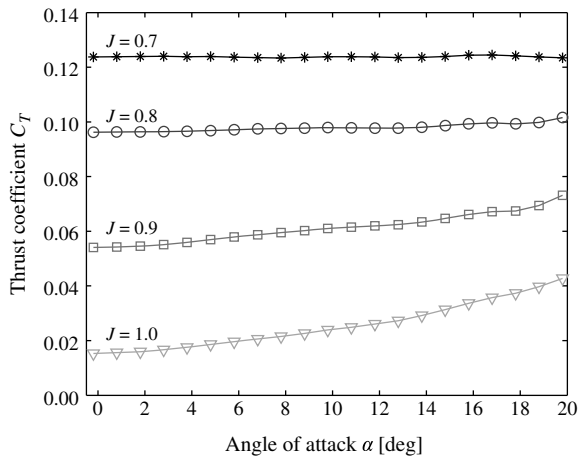


Fig. 10 Effect of angle of attack on the propeller thrust at $Re_D = 620,000$.

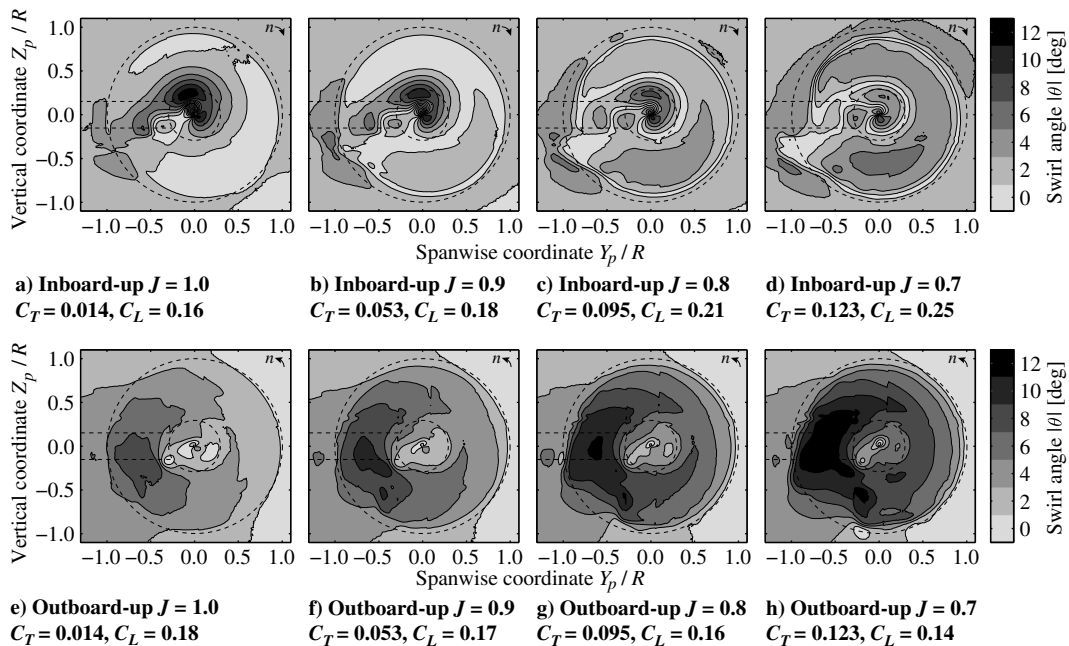


Fig. 11 Absolute swirl angle at $1.5c$ downstream of the wing trailing edge at $\alpha = -0.2$ deg (inboard-up) and $\alpha = +0.2$ deg (outboard-up), rear view.

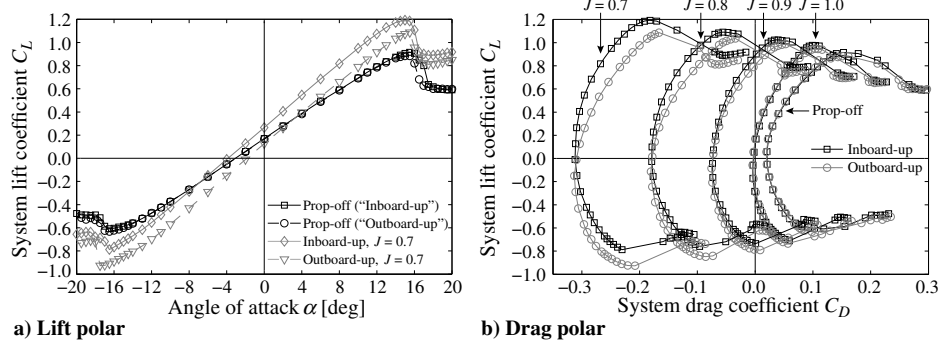


Fig. 12 Lift and drag polars including propeller forces with inboard-up and outboard-up rotation.

the propeller-blade tip vortices [20]. For a model without a flap, this local maximum in swirl would not occur; instead, the swirl would be more spread out over the entire disk.

2. System Performance

The difference in swirl downstream of the model with inboard-up and outboard-up rotation (Fig. 11; Table 3) can be expected to cause a strong offset in system performance between these two cases. This is confirmed by Fig. 12, which displays the lift and drag of the entire system, including propeller forces, with inboard-up and outboard-up rotation. The fact that the propeller-off results for the inboard-up and outboard-up cases (measured with $\delta_f = +10$ deg and $\delta_f = -10$ deg) overlap confirms the symmetry of the setup between the positive and negative flap settings, except at the highest positive angles of attack at which the stall behavior was slightly different for the two cases. This is very likely due to an asymmetry in the model.

In terms of lift (Fig. 12a), the interaction between the propeller slipstream and the wing increases the system performance for the case with inboard-up rotation. With outboard-up propeller rotation, on the other hand, the lift decreases compared to the propeller-off case for angles of attack below approximately 4 deg, and the lift is lower than with inboard-up rotation over the entire angle-of-attack range, including the maximum lift coefficient. The propeller-wing interaction also affects the system drag (Fig. 12b). Again, a clear benefit can be seen for the case with inboard-up rotation. This benefit increases with increasing lift coefficient and thrust setting.

3. Wing Performance

The aerodynamic advantages observed in Fig. 12 for the case with inboard-up rotation are a direct result of the interaction between the propeller slipstream and the wing. To identify the sources of the dominant interaction mechanisms, the local pressure data on the wing were analyzed. In this way, the impact of the interaction effects on the wing performance and propeller performance could be separated. The pressure data were integrated to obtain the section lift and pressure-drag coefficients at eight spanwise stations. Figure 13

presents the resulting lift distributions for the inboard-up and outboard-up rotation cases for all thrust settings considered, at $\alpha = 0$ deg. The wing loading decreased toward the root of the wing ($Y/s_s = 0$) because the flap did not cover the entire span of the wing. This will have modified the lift distribution somewhat when compared to a cambered wing without flap deflection.

Figure 13 confirms that the interaction with the propeller slipstream increases the wing lift with inboard-up rotation and decreases the wing lift with outboard-up rotation. This is due to the difference in upwash experienced by the wing for the two cases, as sketched in Fig. 14. With inboard-up rotation, the wing experiences upwash and higher dynamic pressure on the spanwise part washed by the slipstream (region II in Fig. 14), thereby enhancing the lift compared to the propeller-off case. For the outboard-up rotation case, the direction of the propeller swirl is reversed, causing a downwash contribution to the local wing inflow and a resulting reduction in lift compared to the propeller-off case. The interaction effects are amplified with increasing propeller thrust setting due to the associated increase in swirl and dynamic-pressure rise induced by the propeller.

With the propeller on, a steep lift gradient occurs around the slipstream boundary ($Y/s_s \approx 0.6$). This lift gradient causes vorticity to be shed, which modifies the inflow angle on the spanwise part of the wing not immersed in the propeller slipstream (region I in Fig. 14). As illustrated in Fig. 15a, an upwash occurs with inboard-up rotation and a downwash with outboard-up rotation. Consequently, the local lift increases compared to the propeller-off result with inboard-up rotation (Fig. 13a). The spanwise lift gradient becomes steeper with increasing thrust setting due to the associated increase in swirl and dynamic pressure in the slipstream region. For the case with outboard-up rotation (Fig. 13b), the situation is reversed. However, the spanwise lift gradient is smaller than for the inboard-up rotation case due to the opposing effects of the downwash and increased dynamic pressure in the slipstream (Fig. 14b). Therefore, the modification of the wing lift on the spanwise part of the wing away from the slipstream is smaller with outboard-up rotation than with inboard-up rotation.

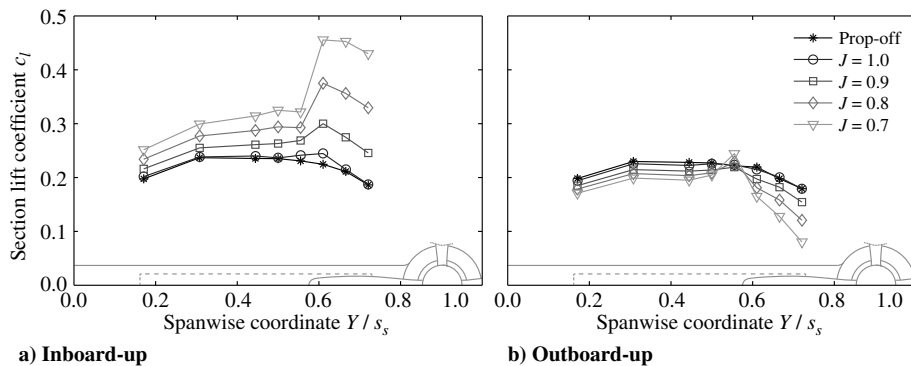


Fig. 13 Effect of propeller thrust setting on the spanwise lift distribution at $\alpha = 0$ deg.

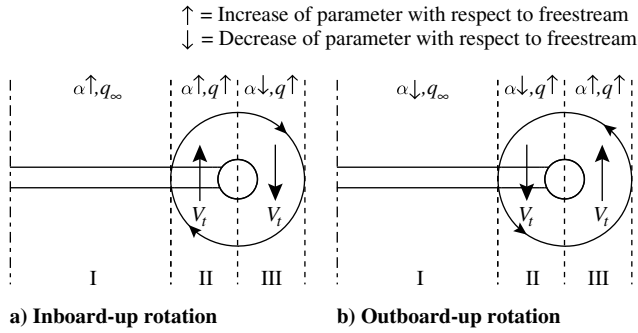


Fig. 14 Sketch of wing-inflow modification due to the propeller.

The shedding of vorticity associated with the spanwise lift gradient also introduces velocities in the spanwise direction (Figs. 15b and 15c), which distort the propeller slipstream during and after its interaction with the wing [8,13,21]. The resulting spanwise shearing of the slipstream is visualized in Fig. 16 by contours of the total-pressure coefficient measured downstream of the models for the cases with inboard-up rotation ($\alpha = -0.2$ deg) and outboard-up rotation ($\alpha = +0.2$ deg). For reference, the propeller-off results are also included; these cases display the expected regions of total-pressure loss

in the wing wake, wingtip vortex, and nacelle wake. Furthermore, the flap-edge vortices can be recognized, which will have led to a reduction in strength of the wingtip vortex. The propeller-on data show that the slipstream moves away from the propeller axis on the advancing blade side and toward the propeller axis on the retreating blade side. This occurs for both the cases with inboard-up and outboard-up rotation, matching the directions of the spanwise flow depicted in Figs. 15b and 15c. The slipstream distortion becomes stronger with increasing thrust setting due to the associated increase of the spanwise lift gradient (Fig. 13).

The spanwise shearing of the slipstream modifies the local wing performance near the slipstream edge. Although this especially affects the unsteady lift and drag response [13,21], also the time-averaged wing loading is altered. This can be seen in Fig. 13b by the sudden increase in lift at $Y/s_s = 0.555$ for the case with outboard-up rotation at the highest thrust coefficient ($J = 0.7$; $C_T = 0.123$). In this condition, the strong spanwise displacement of the slipstream (Fig. 16j) made that at $Y/s_s = 0.555$ part of the wing's suction side was washed by the slipstream, whereas the pressure side was not.

The rise in lift due to the slipstream interaction with inboard-up rotation (Fig. 13a) is mostly due to an increase in loading on the front part of the profile, which becomes more pronounced with increasing thrust setting. This is shown by the pressure distributions provided in Fig. 17, in which the results measured at $J = 1.0$ and $J = 0.8$ are omitted for clarity. The results are given for two spanwise stations: one

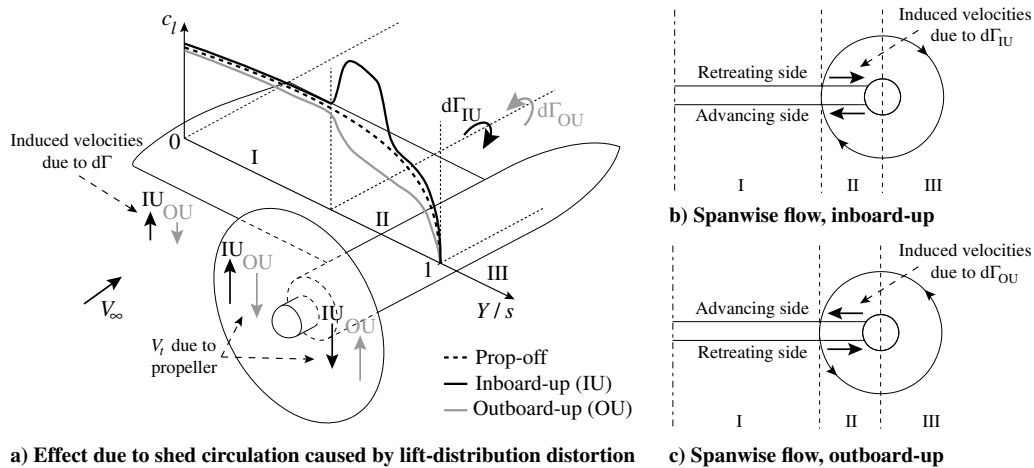


Fig. 15 Sketch explaining the induced velocities due to the spanwise lift gradient at the slipstream edge.

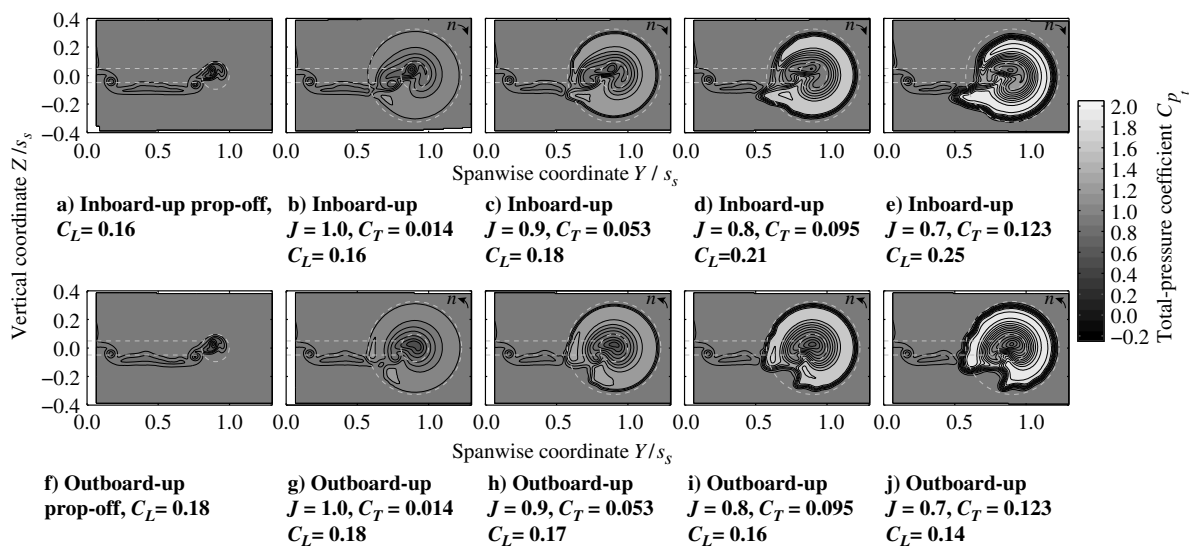


Fig. 16 Slipstream distortion at $\alpha = -0.2$ deg (inboard-up) and $\alpha = +0.2$ deg (outboard-up), rear view.

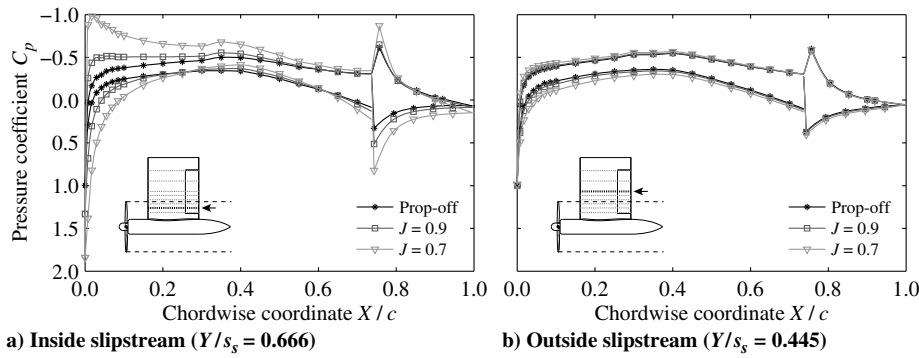


Fig. 17 Effect of propeller thrust setting on the wing pressure distribution at $\alpha = 0$ deg, inboard-up rotation.

inside the slipstream ($Y/s_s = 0.666$) and one outside the slipstream ($Y/s_s = 0.445$). Markers are displayed at the individual sampling locations, whereas the lines indicate the inter- and extrapolated results used as input for the integration procedure applied to compute the sectional lift and pressure drag on the wing. The local jump in the pressure distribution at $X/c = 0.75$ is due to the deflected flap. The effects for the outboard-up rotation case (not shown) were similar but opposite, with a decrease in front loading due to the downwash induced by the propeller (Fig. 14b).

To assess the impact of the propeller on the wing lift under asymmetric inflow conditions, the pressure integration was performed for all considered angles of attack. Figure 18 presents the resulting lift polars at the same spanwise stations as in Fig. 17. Similarly as for the integral forces depicted in Fig. 12, both the inboard-up and outboard-up rotation cases are shown. Only the highest thrust setting $J = 0.7$ ($C_T = 0.123$) is considered here for clarity, together with the propeller-off results. The effects for the intermediate thrust settings were similar, albeit with smaller differences in amplitude compared to the propeller-off case.

The section lift polars plotted in Fig. 18 further substantiate the mechanism sketched in Figs. 14 and 15. The upwash and increased dynamic pressure inside the slipstream experienced with inboard-up rotation increase the sectional lift compared to the propeller-off case over the entire angle-of-attack range. The same effect, although with smaller magnitude, occurs outside of the slipstream due to the induced velocities associated with the spanwise lift gradient on the wing and the decrease in downwash due to the wingtip-vortex attenuation. For the outboard-up rotation case, on the other hand, the propeller swirl is experienced as a downwash, resulting in a loss of lift, which is only partially compensated for by the increased dynamic pressure in the slipstream. The effective downwash induced by the propeller leads to an increase of the stall angle with outboard-up rotation, whereas with inboard-up rotation, the stall angle decreases compared to the propeller-off case. The behavior of the system lift with propeller on, shown before in Fig. 12, falls between the local lift polars measured inside and outside the slipstream. This confirms that the measured change in system lift was due to the local changes to the

wing pressure distribution, which behaved according to the sketches provided in Figs. 14 and 15.

As shown in Fig. 12b, the modification of the up- and downwash experienced by the wing with the propeller on results in clear shifts in the system drag. To relate this to a modification of the wing drag, the pressure data were integrated to obtain polars of the pressure drag as a function of angle of attack, as shown in Fig. 19. Note that these polars do not include the viscous drag term, and therefore, only represent part of the total drag acting on the wing. Furthermore, the integration of the pressure in the drag direction features a relatively high uncertainty, as illustrated by the difference between the propeller-off results obtained from the configurations with opposite flap deflections.

The pressure-drag polars presented in Fig. 19 show that, at positive lift coefficients, the wing performance improves with inboard-up rotation and worsens with outboard-up rotation compared to the case without propeller. Inside the slipstream (region II in Fig. 14), the propeller-induced swirl modifies the wing induced drag by tilting the lift vector. With inboard-up rotation, the propeller swirl is experienced as upwash (Fig. 14a). Therefore, at positive lift coefficients, the lift vector is tilted forward and the induced drag decreases: swirl recovery [8]. Furthermore, the form drag decreases due to the lower angle of attack required to reach a given lift coefficient. With outboard-up rotation, the opposite situation occurs, and the pressure drag increases compared to the propeller-off case. The modification of the wingtip vortex due to the interaction with the propeller slipstream should enhance the swirl-recovery effect. The decrease in downwash occurring with inboard-up rotation reduces the induced drag, whereas with outboard-up rotation the downwash is amplified, and thus, the induced drag increased. At negative lift coefficients, for which the wingtip vortex rotates in the opposite direction, both the swirl-recovery and wingtip-vortex-attenuation mechanisms are reversed, and the case with outboard-up rotation displays the best performance. The trends in the pressure-drag polars shown in Fig. 19 match with the behavior of the system drag presented in Fig. 12b. This confirms that the reduction in system drag for the inboard-up rotation case is directly related to the modification of the swirl by the interaction of the propeller slipstream with the wing.

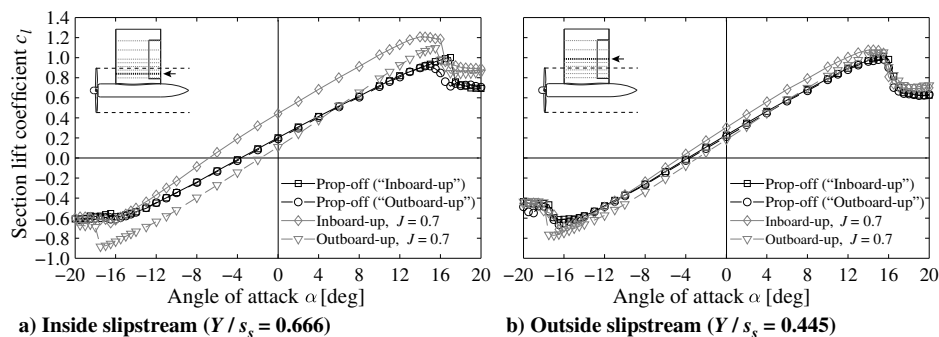


Fig. 18 Effect of propeller thrust setting on the wing's section lift polars.

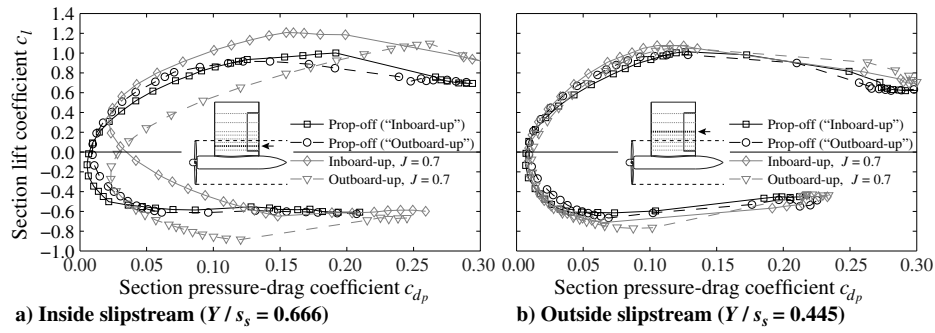


Fig. 19 Effect of propeller thrust setting on the wing's section pressure-drag polars.

Apart from the effects due to swirl, the wing drag is also affected by the modified dynamic pressure in the spanwise part of the wing washed by the propeller slipstream (region II in Fig. 14). The local increase in velocity causes an increase in pressure drag and viscous drag compared to the propeller-off case, with both propeller rotation directions. This is reflected in Fig. 19a by the lower pressure drag for the propeller-off case at small values of the wing lift coefficient ($-0.5 < c_l < 0.4$).

4. Propeller Performance

So far, only the downstream interaction of the propeller slipstream with the wing has been discussed. The upstream effect of the wing on the propeller was quantified by total-pressure measurements taken at $0.15R$ downstream of the propeller plane for the wing-installed configuration. Figure 20 presents contours of the total-pressure rise due to the propeller for the configurations with inboard-up and outboard-up rotation at an advance ratio of $J = 0.8$ ($C_T = 0.095$). The measurements were taken at $\alpha = -0.2$ deg for the inboard-up case and $\alpha = +0.2$ deg for the outboard-up case due to a small misalignment of the model. Combined with the change in slipstream interaction effects for the different rotation directions, this means that the wing lift coefficients were different for the inboard-up ($C_L = 0.21$) and outboard-up ($C_L = 0.16$) cases.

The upstream perturbation of the propeller inflow caused by the wing is due to a combination of blockage and upwash. Independent of the propeller rotation direction, the blockage effect reduces the axial velocity at the propeller plane upstream of the wing, thereby increasing the local blade loading. The upwash affects the effective tangential velocity experienced by the blades when passing by the wing: the tangential velocity decreases with inboard-up rotation and increases with outboard-up rotation. Therefore, the two effects partially cancel for the case with inboard-up rotation. Consequently, for this case, the resulting upstream effect of the wing on the propeller loading is smaller than with outboard-up rotation and peaks somewhat further away from the wing. This can be seen in

Fig. 20 by the smaller increase in loading near the wing for the inboard-up rotation case. For both cases, however, the upstream effect of the wing on the blade loading was limited. Compared to the total-pressure rise measured for the isolated propeller (Fig. 8b), the circumferentially integrated loading increased by 1.7% with inboard-up rotation and 2.3% with outboard-up rotation. The maximum circumferential variations in blade loading were also small, as can be seen in Fig. 21a for both rotation directions. The data are provided for a radial station of $r/R = 0.76$, at which the blade loading was at a maximum, while the circumferential blade position ϕ is defined as in Figs. 3 and 20. With both rotation directions, the maximum perturbation of the blade loading was about 2% of the time-averaged result.

For the inboard-up rotation case, the sensitivity of the blade-loading variations to the propeller thrust setting was assessed by also taking measurements at other advance ratios. Figure 21b shows that the unsteady propeller loading features a nonmonotonic variation with the propeller thrust setting. On the one hand, an increase of the propeller thrust amplifies the downstream wing loading (Fig. 13a), which leads to a stronger perturbation of the propeller inflow due to increased upwash. On the other hand, the sensitivity of the propeller loading to inflow perturbations decreases with increasing thrust setting, as shown by the variation of the isolated propeller's thrust coefficient with angle of attack (Fig. 10). For the current configuration, the maximum unsteady blade loads occurred at $J = 0.9$ ($C_T = 0.053$), for which a maximum change in blade loading was measured of 3% of the time-averaged result. Therefore, it is concluded that, at the considered angle of attack around 0 deg, the upstream effect of the wing on the propeller was small.

No measurements were taken to study the upstream effect of the wing on the propeller loading at nonzero angle of attack (ignoring the 0.2 deg misalignment). However, previous numerical investigations of the same setup [20] showed that at $\alpha = +10$ deg, the relative impact of the upstream effect decreased over the largest part of the

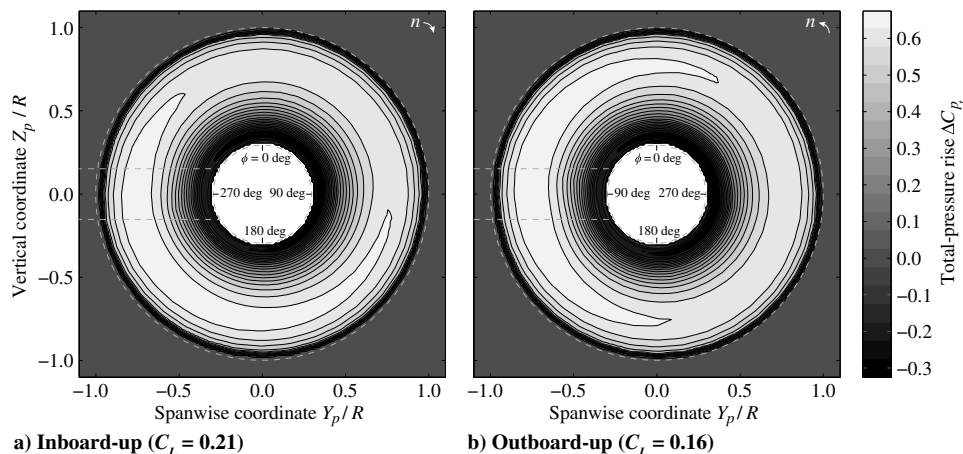


Fig. 20 Total-pressure rise at $J = 0.8$ ($C_T = 0.095$), $\alpha = -0.2$ deg (inboard-up) and $\alpha = +0.2$ deg (outboard-up), rear view.

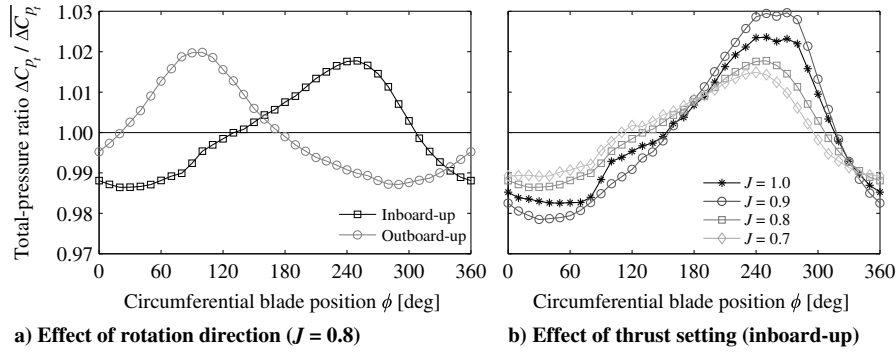


Fig. 21 Circumferential variation of total-pressure rise at $r/R = 0.76$, $\alpha = -0.2$ deg (inboard-up) and $\alpha = +0.2$ deg (outboard-up).

blade span when compared to the case at $\alpha = 0$ deg. For the latter, Ref. [20] predicted an increase in propeller loading of around 3% due to the presence of the wing, which is slightly more than measured in the experiments discussed in the present paper.

C. Aerodynamic Performance Comparison of Conventional and Wingtip-Mounted Configurations (Model 2)

The aerodynamic interaction effects for wingtip-mounted propellers discussed in the previous section show the potential for significant performance benefits due to wingtip-vortex attenuation and swirl recovery. To illustrate the potential aerodynamic performance gain of the wingtip-mounted propeller, a direct comparison was made with the conventional configuration, with the propeller mounted on the inboard part of the wing. For this comparison, model 2 was used (modular cambered wing; see Figs. 4–6). The traversable wake rake was employed first to highlight the differences in wake and slipstream flowfield between the two configurations. Subsequently, the system and wing performance were evaluated based on measurements with the external balance. All data were acquired at $Re_D = 640,000$, unless noted otherwise, while the propeller rotation direction was always inboard-up. The data are attached to this paper as Supplemental Data S6.

1. Wake and Slipstream Flowfield

The flowfield in the wake of the conventional and wingtip-mounted configurations was visualized by means of contours of the total pressure at 1.5 times the chord length downstream of the wing trailing edge. Figure 22 compares the results obtained without the propeller present. To allow for a fair comparison between the two configurations, the measurements were taken at a constant lift coefficient of $C_L = 0.5$, which was selected to be representative of a typical wing loading in cruise conditions. This lift coefficient was achieved at $\alpha = 2.8$ deg for the conventional configuration and $\alpha = 2.9$ deg for the wingtip-mounted configuration. The dashed lines

indicate the projection of the model geometry onto the measurement plane (at $\alpha = 0$ deg).

For both configurations, the viscous wake of the wing can be recognized by the wide region of total-pressure loss below the projected chord line. The wake displaces downward due to the downwash created by the lifting wing, and rolls up into a wingtip vortex, which features a strong total-pressure deficit due to the local viscous losses. The region of total-pressure loss at the wingtip is more spread out for the wingtip-mounted configuration due to the addition of the viscous losses associated with the nacelle. This is further strengthened by the complex flowfield in the wing–nacelle junction, which, at this angle of attack, seems to have led to flow separation inboard of the nacelle. Compared to the conventional configuration, the tip-vortex location for the wingtip-mounted configuration was positioned somewhat more inboard ($Y/s_t = 0.949$ vs $Y/s_c = 0.955$). This is a result of the slightly higher aspect ratio for the conventional configuration due to the addition of the rounded wingtip. For both configurations, the boundary layer on the ground board is visible near $Y/s = 0$, with a flow pattern typical of the junction flow at the interface of a wing and a flat plate [22,23].

As shown before in Fig. 16, the operation of the propeller causes a strong modification of the wake flowfield. Figure 23 provides total-pressure contours for the conventional and wingtip-mounted configurations for the case with the propeller running at $J = 0.7$ ($C_T = 0.123$). As for the propeller-off results shown in Fig. 22, the data were acquired at a constant lift coefficient of $C_L = 0.5$. The corresponding angles of attack were $\alpha = 2.0$ deg for the conventional configuration and $\alpha = 1.9$ deg for the wingtip-mounted configuration. Note that the scale of the contour levels is different from the one used in Fig. 22.

The total-pressure contours plotted in Fig. 23 display the expected spanwise shearing of the propeller slipstream due to its interaction with the wing. The spanwise velocities are as illustrated in Fig. 15, displacing the propeller slipstream away from the propeller axis on the advancing blade side and toward the propeller axis on the

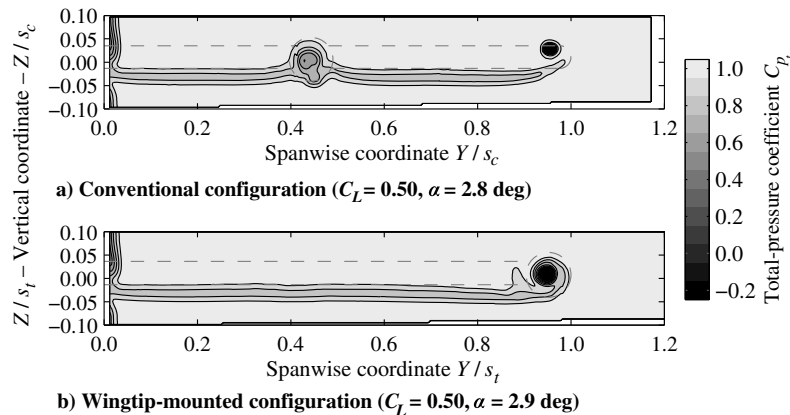


Fig. 22 Wake flowfield without propeller, rear view.

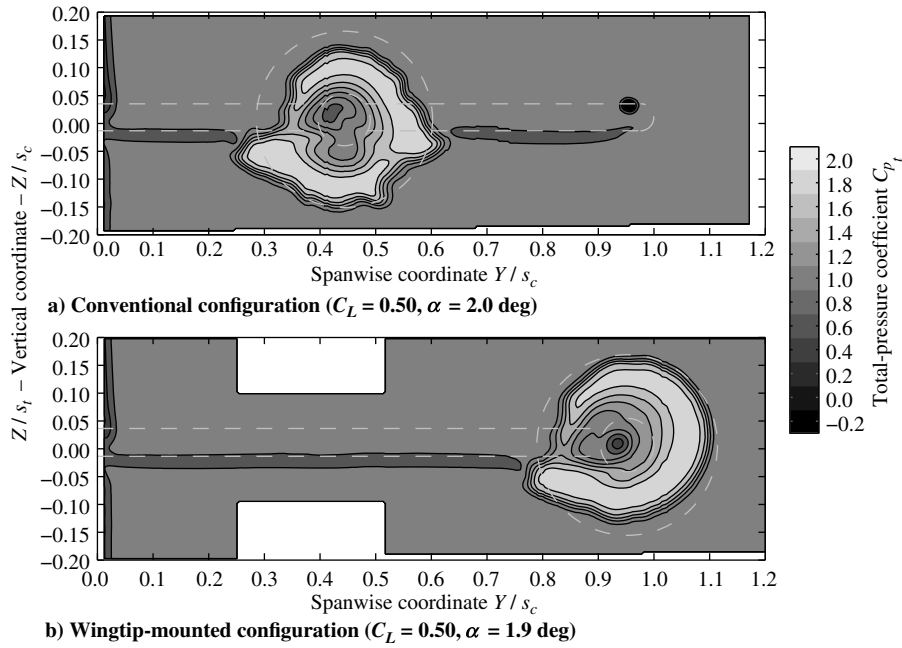


Fig. 23 Slipstream distortion at $J = 0.7$ ($C_T = 0.123$), rear view.

retreating blade side. The slipstream distortion is most pronounced for the conventional configuration, because it occurs on both the inboard and outboard sides of the nacelle. For the wingtip-mounted configuration, the outboard part of the slipstream remains approximately circular, because it is away from the wing. The vertical position of the slipstream is about $0.15R$ higher for the wingtip-mounted configuration than for the conventional configuration. This is due to the lower downwash near the tip of the wing. In both cases, the flow topology around the nacelle and away from the propeller slipstream is similar to that observed for the propeller-off case in Fig. 22.

The slipstream distortion for the wingtip-mounted configuration (Fig. 23b) was less pronounced than that shown before for model 1 at the same propeller thrust setting (Fig. 16e). This is because the diameter-to-span ratio was smaller for model 2 than for model 1, leading to a smaller perturbation of the wing lift distribution by the propeller at a given thrust coefficient. As a result, the displacement of the slipstream was decreased, following the mechanism sketched in Fig. 15. Moreover, the results for model 1 may have featured an additional distortion of the slipstream near the flap edge, which did not occur with model 2.

2. System Performance

The external balance was used to quantify the aerodynamic performance of the conventional and wingtip-mounted configurations. In this section, the lift and drag of the entire system are

considered, including propeller forces. Figure 24 compares the lift and drag polars measured for both configurations as a function of propeller thrust setting.

The lift polars plotted in Fig. 24a show little difference between the lift performance of the conventional and wingtip-mounted configurations. At higher angles of attack, the conventional configuration provided a slightly higher lift than the wingtip-mounted configuration. This may have been due to the local upwash introduced on both sides of the nacelle when it is subjected to a positive angle of attack. For the conventional configuration, this affects the wing lift on both sides of the nacelle, resulting in a larger lift increase than for the wingtip-mounted configuration. For that configuration, only the lift on the inboard side of the nacelle is impacted.

As discussed in Sec. III.B.3, the effect of the propeller is to increase the lift for the wingtip-mounted configuration due to the locally increased dynamic pressure and inflow angle caused by the propeller slipstream. Similar effects occur for the conventional configuration [5,8], as sketched in Fig. 25. The propeller-induced upwash increases the angle of attack and dynamic pressure on the inboard part of the wing immersed in the slipstream (region II). On the outboard part of the wing immersed in the slipstream (region III), on the other hand, the propeller causes a downwash, which decreases the local angle of attack. This is partially offset by the local increase in dynamic pressure. The resulting spanwise lift gradients at the edges of regions 2 and 3 cause induced velocities, which also modify the local angle of attack on the parts of the wing not immersed in the propeller

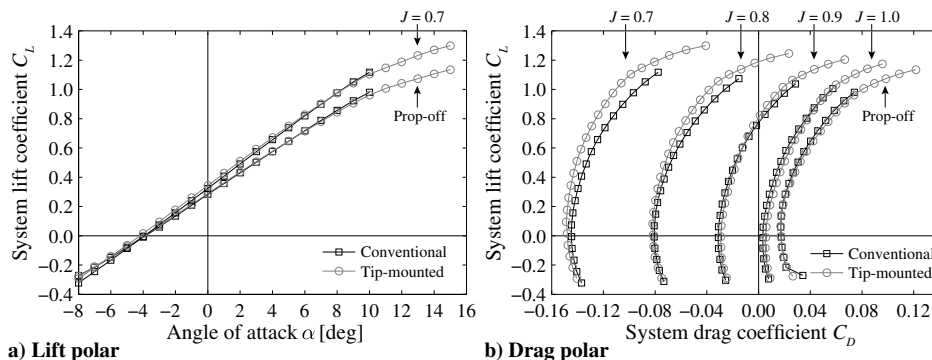


Fig. 24 Lift and drag polars of the conventional and wingtip-mounted configurations, including propeller forces.

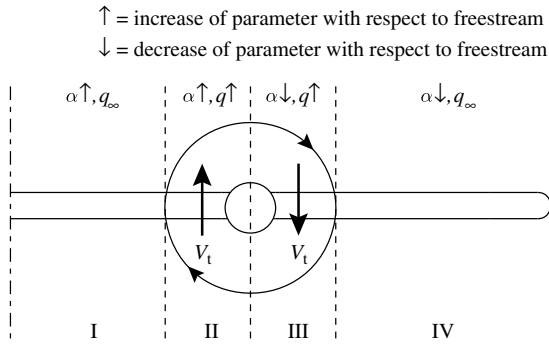


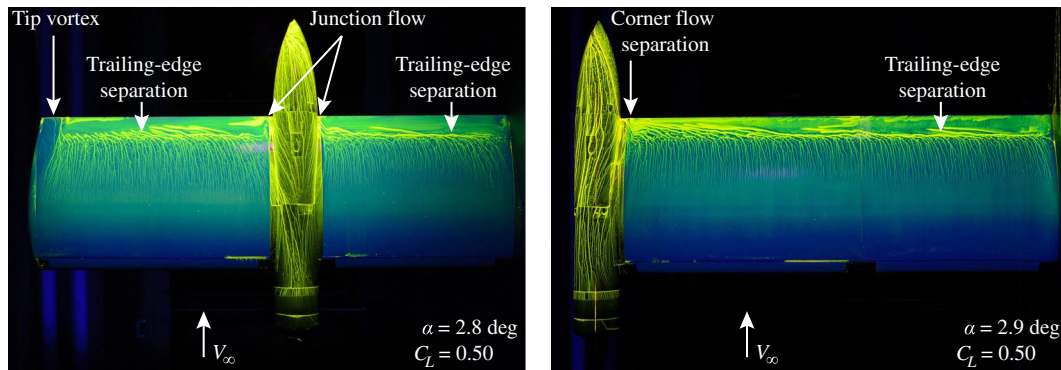
Fig. 25 Wing-inflow modification due to the propeller for conventional configuration with inboard-up rotation.

slipstream. On the inboard part (region I), the angle of attack increases, whereas on the outboard part (region IV), the angle of attack decreases.

Whereas the conventional and wingtip-mounted configurations produced an approximately equal lift, the system drag (Fig. 24b) reveals an increasing drag benefit for the wingtip-mounted configuration with increasing propeller thrust setting. Note that the thrust force, which is negative in the drag direction, is included in the plotted drag coefficient. Therefore, more negative values of the drag coefficient indicate better system performance at a given lift coefficient and propeller setting. For the propeller-off condition at positive lift coefficients, the conventional configuration showed a slightly lower drag than the wingtip-mounted configuration. This was an unexpected result, seeing that for the wingtip-mounted configuration the nacelle acts as a wingtip device, which should lead to a lower induced drag. However, this may

have been offset by the slightly higher geometric aspect ratio of the conventional configuration. Furthermore, the upwash induced by the nacelle, discussed before, may have led to a reduction of the lift-induced drag for the conventional configuration. For both configurations, trailing-edge separation was present at all angles of attack above 0 deg, as indicated by the oil-flow images shown in Fig. 26. This was due to the modification of the trailing-edge geometry, discussed before in Sec. II.B.2, which was required for manufacturing reasons. For the wingtip-mounted configuration, corner flow separation can be observed near the wing-nacelle junction, explaining the local total-pressure loss seen before in Fig. 22b. The images recorded at higher angles of attack (not shown here) displayed a particularly complex flow topology around the wing-nacelle junctions for the conventional configuration. Apparently, this did not lead to a noticeable drag penalty compared to the wingtip-mounted configuration.

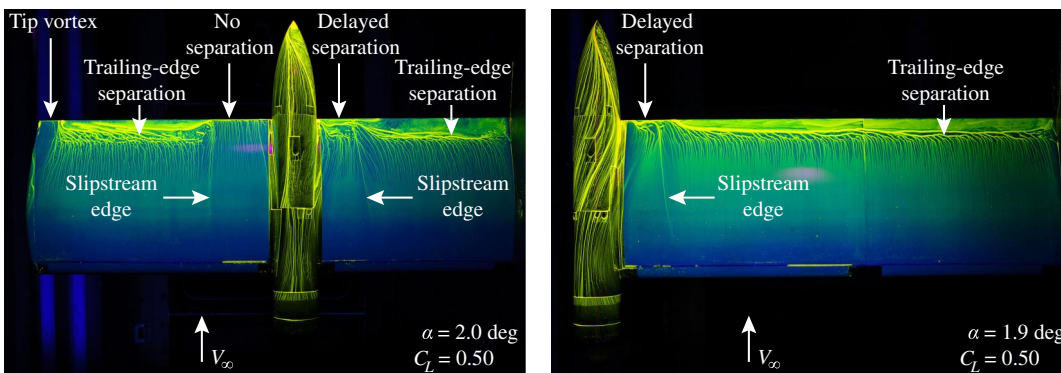
With the propeller running, clear shifts occurred in the drag polars. For the conventional configuration, the upwash and downwash on the inboard and outboard parts of the wing (Fig. 25) modified the wing induced drag by tilting the lift vector forward and backward. Furthermore, the lower effective angle of attack on the outboard segment of the wing immersed in the slipstream (region III in Fig. 25) eliminated or delayed the trailing-edge separation occurring without the propeller present, as shown by the oil-flow images depicted in Fig. 27. This was further amplified by the increased Reynolds number associated with the increased velocity in the slipstream, which also delayed the separation on the inboard side of the wing. On the other hand, the higher velocity experienced by the parts of the wing immersed in the propeller slipstream leads to an increase in drag compared to the propeller-off case, as discussed in Sec. III.B.3. The relative magnitude of the aforementioned mechanisms depends on the propeller efficiency, propeller-diameter-to-span ratio, Reynolds number, wing zero-lift drag coefficient, and wing lift coefficient. The



a) Conventional configuration

b) Wingtip-mounted configuration

Fig. 26 Oil-flow visualizations of the surface flow with propeller off, top view.



a) Conventional configuration

b) Wingtip-mounted configuration

Fig. 27 Oil-flow visualizations of the surface flow with propeller on ($J = 0.7$; $C_T = 0.123$), top view.

Reynolds-number effect would be less pronounced at full scale than in the wind tunnel. At full scale, the absolute value of the Reynolds number would be higher, and thus, the local effect of the Reynolds-number increase by the propeller would be less relevant. For the wingtip-mounted configuration, the effects are as discussed in Sec. III.B.3. The combination of wingtip-vortex attenuation and swirl recovery reduces the induced drag of the wing when the propeller is operated with inboard-up rotation.

Figure 24b shows that the drag reduction offered by the wingtip-mounted configuration becomes increasingly dominant with increasing propeller thrust setting. At $J = 0.8$ and $J = 0.7$, clear induced-drag benefits can be seen when compared to the conventional configuration. This is confirmed by Fig. 28, which displays the change in drag of the wingtip-mounted configuration compared to the conventional configuration as a function of the propeller thrust coefficient and system lift coefficient. Note that negative numbers for the drag delta ΔC_{D_i} indicate a drag benefit for the wingtip-mounted configuration. The data measured at $Re_D = 450,000$ are also included, thereby extending the range of thrust conditions considered to $C_T = 0.168$ (at $J = 0.5$). The data points at $C_T = 0$ were obtained with the blades removed, and thus, are representative of the propeller-off case.

Figure 28 highlights the sensitivity of the drag benefit of the wingtip-mounted configuration to the propeller thrust setting. As discussed before, for the propeller-off case, the drag was higher for the wingtip-mounted configuration than for the conventional configuration, which is reflected in Fig. 28 by the positive values of ΔC_{D_i} at $C_T = 0$. For lift coefficients below around $C_L = 0.7$, this drag benefit of the conventional configuration initially increased at the lowest propeller thrust setting. This could be due to the elimination of flow separation on the outboard part of the wing washed by the slipstream, as discussed before, which may have also occurred at the lowest thrust setting. The drag penalty of the wingtip-mounted configuration then gradually turned into a drag reduction with increasing propeller thrust setting. For the tested geometry, drag reductions of 15–40 counts were achieved with the wingtip-mounted configuration compared to the conventional configuration at $C_L = 0.5$ and $0.09 < C_T < 0.13$ ($0.7 < J < 0.8$), corresponding to an overall drag reduction of 5–15%. The drag benefit of the wingtip-mounted configuration further increases upon increasing the system lift coefficient and propeller thrust setting. For thrust settings of $0.14 < C_T < 0.17$ ($0.5 < J < 0.6$) and a lift coefficient of $C_L = 0.7$, drag reductions of 100–170 counts (25–50%) were measured. It should be noted that these values are specific to the tested configuration. Still, they confirm a strong potential for drag reductions by the wingtip-mounted configuration due to the wingtip-vortex-attenuation mechanism.

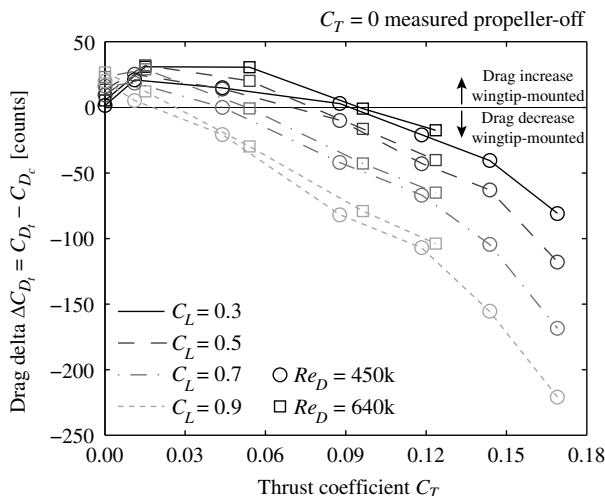


Fig. 28 Drag benefit of wingtip-mounted configuration compared to conventional configuration.

3. Wing Performance

The propeller forces discussed in Sec. III.A were removed from the system performance data presented in Fig. 24 to study the effect of the propeller on the performance of the wing with nacelle. At each angle of attack, the propeller performance was subtracted as measured with the sting-mounted propeller setup at that same angle of attack. Therefore, the procedure accounts for the change in propeller normal force and thrust with angle of attack. However, the upstream effect of the wing on the propeller performance is neglected. This was considered acceptable based on the discussion of Sec. III.B.4. The data with propeller forces subtracted were used to determine the wing's lift-curve slope C_{L_α} and span-efficiency parameter e for the conventional and wingtip-mounted configurations, as a function of the propeller thrust setting.

The lift-curve slope was obtained by fitting a first-order polynomial through the $C_L - \alpha$ data for an angle-of-attack range of $-8 \leq \alpha \leq +8$ deg. An estimate of the error of the fitting procedure was made by statistical analysis. The procedure was repeated 5000 times, each time with a random error (based on a normal distribution with standard deviation equal to the known uncertainty of the balance data) superimposed on the lift data. The standard deviation of the 5000 tests was then taken as the uncertainty of the determined lift-curve slope. Figure 29 displays the results as a function of the propeller thrust coefficient, for both the conventional and wingtip-mounted configurations. The data points at $C_T = 0$ again represent the propeller-off case, as measured without blades. The uncertainty (approximately $2 \cdot 10^{-5}$ / deg) is indicated by error bars surrounding the individual data points.

Figure 29 shows that, at the propeller-off condition, the lift-curve slope was higher for the conventional configuration than for the wingtip-mounted configuration. This may have been due to the upwash induced by the nacelle when operating at nonzero angle of attack, as discussed before in relation to Fig. 24. Decreasing the Reynolds number from $Re_D = 640,000$ to $Re_D = 450,000$ led to a reduction of the lift-curve slope. The increase in boundary-layer thickness with a decrease in Reynolds number causes a stronger effective decambering of the wing profile, thereby, worsening the lift performance.

The lift-curve slope increased with increasing thrust coefficient for both the conventional and wingtip-mounted configurations due to the combination of the dynamic-pressure rise and swirl in the slipstream, as discussed before. At the maximum thrust setting considered ($J = 0.5$; $C_T = 0.168$), the propeller effect increased the lift-curve slope by 14% for the conventional configuration and 10% for the wingtip-mounted configuration. At thrust settings more representative of cruise conditions for the tested configuration ($0.7 < J < 0.8$; $0.09 < C_T < 0.13$), this decreased to 4–7% for the conventional configuration and 3–5% for the wingtip-mounted configuration. The

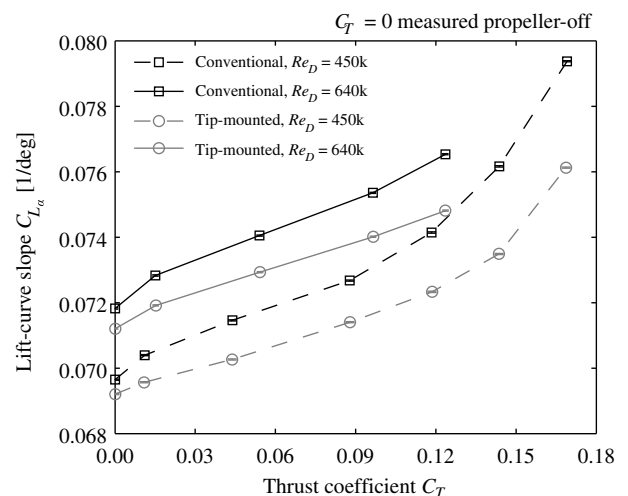


Fig. 29 Lift-curve slope of the wing with nacelle for the conventional and wingtip-mounted configurations.

larger changes for the conventional configuration are because the increased dynamic pressure in the propeller slipstream affects a larger part of the wing than for the wingtip-mounted configuration (see Fig. 25 vs Fig. 14a), and acts on the inboard part of the wing where the section lift is higher than near the wingtip. Apparently, this was sufficient to offset the higher span efficiency of the wing for the wingtip-mounted configuration shown below. The relative change of the lift-curve slope due to the propeller effect was approximately equal at the two Reynolds numbers considered.

The drag polars displayed in Fig. 24b already indicated that the wingtip-mounted configuration offers an induced-drag benefit compared to the conventional configuration. To verify the sensitivity of this induced-drag benefit to the propeller thrust coefficient, the span-efficiency parameter e of the wing with nacelle was derived from the drag data with propeller forces removed. To this end, a parabolic relation was assumed between the drag coefficient and the lift coefficient:

$$C_D = C_{D_{\min}} + \frac{1}{\pi Re} (C_L - C_{L_{C_{D_{\min}}}})^2 \quad (2)$$

To extract the value of the span-efficiency parameter e , the $C_L - C_D$ data were first interpolated. After subtracting the minimum drag coefficient from Eq. (2), a linear curve was fit to obtain the value of e . The uncertainty was again obtained from a statistical analysis with 5000 evaluations. The procedure was relatively sensitive to scatter in the input data, as indicated by the computed uncertainty of approximately 0.05–0.09. Figure 30 presents the evolution of the span-efficiency parameter with the propeller thrust coefficient, for the conventional and wingtip-mounted configurations. The reference results obtained with the propeller blades removed are again indicated by the data points at $C_T = 0$.

Figure 30 shows that the span efficiency was higher for the conventional configuration than for the wingtip-mounted configuration for the case without the propeller. This matches with the induced-drag benefit observed for the conventional configuration in Fig. 24b. Despite the relatively high uncertainty, significant differences occurred between the two configurations when the propeller was operated. For the conventional configuration, the beneficial effects due to swirl recovery (forward tilting of the wing lift vector) are countered by the decrease in span efficiency caused by the distorted wing lift distribution. As a result, a nonmonotonic behavior of the span-efficiency factor with thrust coefficient is observed. The span efficiency of the wing remained constant (within the uncertainty) for thrust coefficients up to $C_T = 0.09$, but then reached a maximum at $C_T = 0.123$ ($J = 0.7$). At this thrust setting, an increase in span efficiency of approximately 15% was computed compared to the propeller-off condition. At higher thrust coefficients, the span efficiency dropped again, reaching a level about 15% below the

propeller-off result at a thrust coefficient of $C_T = 0.168$ ($J = 0.5$). Although an offset can be observed between the span-efficiency parameters measured at $Re_D = 450,000$ and $Re_D = 640,000$, the relative effects due to the propeller were comparable at both Reynolds numbers.

For the wingtip-mounted configuration, the swirl recovery and attenuation of the wingtip vortex led to significant induced-drag benefits. Combined with the smaller distortion of the wing lift distribution, the effect of the propeller was to increase the span-efficiency parameter with increasing thrust coefficient, except at the highest thrust setting considered. Relative to the propeller-off result, the changes in span efficiency due to the propeller were in the range of 20–40% in the advance-ratio range $0.6 < J < 0.9$ ($0.05 < C_T < 0.15$). The decrease in span efficiency at $C_T = 0.168$ ($J = 0.5$) could be due to the increased distortion of the wing lift distribution caused by the high swirl and dynamic pressure in the propeller slipstream at this condition.

IV. Conclusions

This paper has presented an experimental analysis of the aerodynamic interaction effects for wingtip-mounted propellers. By positioning the propeller at the tip of the wing, the slipstream interacts with the flow around the wingtip, thus affecting the rollup and downstream behavior of the wingtip vortex. PIV measurements downstream of a propeller–wing model showed that this leads to a reduction in overall swirl with inboard-up rotation, in which case the swirl in the slipstream is opposite to that associated with the wingtip vortex. At the same time, the system performance was found to improve due to a reduction of the wing induced drag, leading to the conclusion that the decrease in swirl causes a reduction in downwash experienced by the wing.

Apart from the change in drag, the interaction of the wing with the propeller slipstream also modifies the wing lift. The locally enhanced dynamic pressure increases the lift over the spanwise part of the wing washed by the slipstream, which is amplified by the induced swirl for the case with inboard-up rotation. As a result, a strong spanwise variation in lift occurs with the propeller on. The induced velocities caused by this lift gradient lead to a spanwise shearing of the slipstream. With outboard-up rotation, the swirl in the slipstream acts to locally oppose the increase in wing lift due to the propeller-induced dynamic-pressure rise. Compared to the inboard-up rotation case, this leads to a reduction in wing lift at a given angle of attack, and thus, also a reduction in maximum lift coefficient. Furthermore, the direction of the spanwise shearing of the propeller slipstream is inverted on both sides of the wing.

To quantify the potential aerodynamic benefits of the wingtip-mounted configuration, a direct comparison was made with a conventional configuration, with the propeller mounted on the inboard part of the wing. The increase in wing lift due to the interaction with the propeller was 1–4% smaller for the wingtip-mounted configuration than for the conventional configuration. For the latter, the enhanced dynamic pressure and swirl in the slipstream act over double the spanwise extent and on a part of the wing where the section lift is higher than for the wingtip-mounted configuration. At higher angles of attack, the lift advantage for the conventional configuration could be further enhanced by the local angle-of-attack increase in proximity to both sides of the nacelle.

In terms of drag performance, on the other hand, the wingtip-mounted configuration showed superior performance. At a wing lift coefficient of $C_L = 0.5$ and a thrust coefficient of $0.09 < C_T < 0.13$, the drag reduction amounted to about 15–40 counts (5–15%) compared to the conventional configuration. The aerodynamic benefit of the wingtip-mounted configuration further increases with increasing wing lift coefficient and propeller thrust coefficient, leading to a drag reduction of 100–170 counts (25–50%) at $C_L = 0.7$ and $0.14 < C_T < 0.17$. An analysis of the wing performance confirmed that this drag benefit is mostly due to a reduction of the wing induced drag. Compared to the conventional configuration, a relative increase in span efficiency of up to 40% was measured for the wingtip-mounted configuration. Although the exact drag benefit will

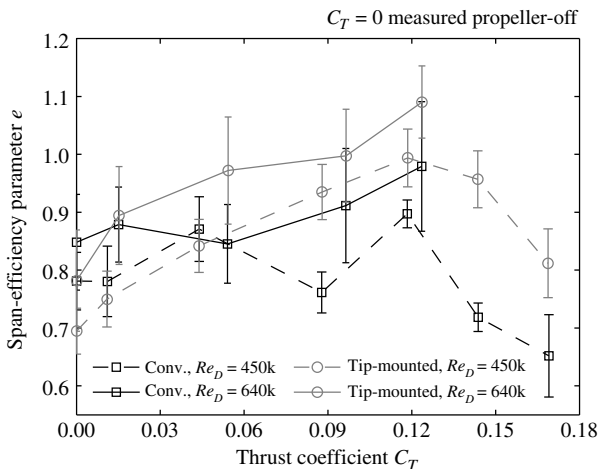


Fig. 30 Span-efficiency parameter of the wing with nacelle for the conventional and wingtip-mounted configurations.

be specific to vehicle design and operating conditions, it is concluded that the interaction between the propeller slipstream and the wingtip vortex leads to a clear drag reduction for the wingtip-mounted configuration. Multidisciplinary analyses are required to evaluate the resulting impact on the potential performance benefits at aircraft level.

Acknowledgments

This work was partially funded by the European Union's Clean Sky 2 Large Passenger Aircraft program under grant agreement number CS2-LPA-GAM-2014-2015-01. The authors would like to thank Stefan Bernardy and Leo Molenwijk for their technical assistance in the preparation and execution of the test campaign, Daniele Ragni for his help during the acquisition and processing of the particle-image-velocimetry data, and Luuk Koomen for designing the modular cambered wing model.

References

- [1] Friedrich, C., and Robertson, P. A., "Hybrid-Electric Propulsion for Aircraft," *Journal of Aircraft*, Vol. 52, No. 1, 2015, pp. 176–189. doi:10.2514/1.C032660
- [2] Moore, M. D., and Fredericks, B., "Misconceptions of Electric Propulsion Aircraft and Their Emergent Aviation Markets," *52nd Aerospace Sciences Meeting*, AIAA Paper 2014-0535, Jan. 2014. doi:10.2514/6.2014-0535
- [3] Stoll, A. M., Bevirt, J., Moore, M. D., Fredericks, W. J., and Borer, N. K., "Drag Reduction Through Distributed Electric Propulsion," *14th AIAA Aviation Technology, Integration, and Operations Conference*, AIAA Paper 2014-2851, June 2014. doi:10.2514/6.2014-2851
- [4] Borer, N. K., Patterson, M. D., Viken, J. K., Moore, M. D., Clarke, S., Redifer, M. E., Christie, R. J., Stoll, A. M., Dubois, A., and Bevirt, J., et al., "Design and Performance of the NASA SCEPTOR Distributed Electric Propulsion Flight Demonstrator," *16th AIAA Aviation Technology, Integration, and Operations Conference*, AIAA Paper 2016-3920, June 2016. doi:10.2514/6.2016-3920
- [5] Witkowski, D. P., Lee, A. K. H., and Sullivan, J. P., "Aerodynamic Interaction Between Propellers and Wings," *Journal of Aircraft*, Vol. 26, No. 9, 1989, pp. 829–836. doi:10.2514/3.45848
- [6] Fratello, G., Favier, D., and Maresca, C., "Experimental and Numerical Study of the Propeller/Fixed Wing Interaction," *Journal of Aircraft*, Vol. 28, No. 6, 1991, pp. 365–373. doi:10.2514/3.46036
- [7] Chieramonte, J. Y., Favier, D., Maresca, C., and Agnes, A., "Unsteady Interactional Effects Between a Propeller and a Fixed Wing," *9th Applied Aerodynamics Conference*, AIAA Paper 1991-3231, Sept. 1991. doi:10.2514/6.1991-3231
- [8] Veldhuis, L. L. M., "Propeller Wing Aerodynamic Interference," Ph.D. Thesis, Faculty of Aerospace Engineering, Delft Univ. of Technology, Delft, The Netherlands, 2005.
- [9] Snyder, M. H., Jr., and Zumwalt, G. W., "Effects of Wingtip-Mounted Propellers on Wing Lift and Induced Drag," *Journal of Aircraft*, Vol. 6, No. 5, 1969, pp. 392–397. doi:10.2514/3.44076
- [10] Miranda, L. R., and Brennan, J. E., "Aerodynamic Effects of Wingtip-Mounted Propellers and Turbines," *4th Applied Aerodynamics Conference*, AIAA Paper 1986-1802, June 1986. doi:10.2514/6.1986-1802
- [11] Patterson, J. C., Jr., and Bartlett, G. R., "Evaluation of Installed Performance of a Wing-Tip-Mounted Pusher Turboprop on a Semispan Wing," NASA TP-2739, Aug. 1987.
- [12] Janus, J. M., Chatterjee, A., and Cave, C., "Computational Analysis of a Wingtip-Mounted Pusher Turboprop," *Journal of Aircraft*, Vol. 33, No. 2, 1996, pp. 441–444. doi:10.2514/3.46959
- [13] Sinnige, T., de Vries, R., Della Corte, B., Avallone, F., Ragni, D., Eitelberg, G., and Veldhuis, L. L. M., "Unsteady Pylon Loading Caused by Propeller-Slipstream Impingement for Tip-Mounted Propellers," *Journal of Aircraft*, Vol. 55, No. 4, 2018, pp. 1605–1618. doi:10.2514/1.C034696
- [14] Yang, Y., Sciacchitano, A., Veldhuis, L. L. M., and Eitelberg, G., "Analysis of Propeller-Induced Ground Vortices by Particle Image Velocimetry," *Journal of Visualization*, Vol. 21, No. 1, 2018, pp. 39–55. doi:10.1007/s12650-017-0439-1
- [15] Scarano, F., and Riethmuller, M. L., "Iterative Multigrid Approach in PIV Image Processing with Discrete Window Offset," *Experiments in Fluids*, Vol. 26, No. 6, 1999, pp. 513–523. doi:10.1007/s003480050318
- [16] Wieneke, B., "PIV Uncertainty Quantification from Correlation Statistics," *Measurement Science and Technology*, Vol. 26, No. 7, 2015, Paper 074002. doi:10.1088/0957-0233/26/7/074002
- [17] Chue, S. H., "Pressure Probes for Fluid Measurement," *Progress in Aerospace Sciences*, Vol. 16, No. 2, 1975, pp. 147–223. doi:10.1016/0376-0421(75)90014-7
- [18] Loving, D. L., and Katzoff, S., "The Fluorescent-Oil Film Method and Other Techniques for Boundary-Layer Flow Visualization," NASA MEMO-3-17-59L, March 1959.
- [19] Stokkermans, T. C. A., van Arnhem, N., Sinnige, T., and Veldhuis, L. L. M., "Validation and Comparison of RANS Propeller Modeling Methods for Tip-Mounted Applications," *2018 AIAA Aerospace Sciences Meeting*, AIAA Paper 2018-0542, Jan. 2018. doi:10.2514/6.2018-0542
- [20] van Arnhem, N., Sinnige, T., Stokkermans, T. C. A., Eitelberg, G., and Veldhuis, L. L. M., "Aerodynamic Interaction Effects of Tip-Mounted Propellers Installed on the Horizontal Tailplane," *2018 AIAA Aerospace Sciences Meeting*, AIAA Paper 2018-2052, Jan. 2018. doi:10.2514/6.2018-2052
- [21] Johnston, R. T., and Sullivan, J. P., "Unsteady Wing Surface Pressures in the Wake of a Propeller," *Journal of Aircraft*, Vol. 30, No. 5, 1993, pp. 644–651. doi:10.2514/3.46393
- [22] Fleming, J. L., Simpson, R. L., Cowling, J. E., and Devenport, W. J., "An Experimental Study of a Turbulent Wing-Body Junction and Wake Flow," *Experiments in Fluids*, Vol. 14, No. 5, 1993, pp. 366–378. doi:10.1007/BF00189496
- [23] Gand, F., Deck, S., Brunet, V., and Sagaut, P., "Flow Dynamics Past a Simplified Wing Body Junction," *Physics of Fluids*, Vol. 22, No. 11, 2010, Paper 115111. doi:10.1063/1.3500697